A&A 569, A41 (2014)
DOI: 10.1051/0004-6361/201423525

Astronomy & Astrophysics

The globular cluster system of NGC 1316

III. Kinematic complexity⋆,⋆⋆

T. Richtler[1], M. Hilker[2], B. Kumar[3], L.P. Bassino[4], M. Gómez[5], and B. Dirsch[6]

[1] Departamento de Astronomía, Universidad de Concepción, Casilla 160-C, Concepción, Chile
e-mail: tom@astro-udec.cl
[2] European Southern Observatory, Karl-Schwarzschild-Str. 2, 85748 Garching, Germany
[3] Aryabhatta Research Institute of Observational Sciences, Manora Peak, 263129 Nainital, India
[4] Grupo de Investigación CGGE, Facultad de Ciencias Astronómicas y Geofísicas, Universidad Nacional de La Plata, and Instituto de Astrofísica de La Plata (CCT La Plata – CONICET, UNLP), Paseo del Bosque S/N, B1900FWA La Plata, Argentina
[5] Departamento de Ciencias Físicas, Facultad de Ciencias Exactas, Universidad Andres Bello, Santiago, Chile
[6] Friedrich-Ebert Gymnasium, Ollenhauerstr. 5, 53113 Bonn, Germany

Received 28 January 2014 / Accepted 8 June 2014

ABSTRACT

Context. The merger remnant NGC 1316 (Fornax A) is one of the most important objects regarding the investigation of and thus an important object to study merger-related processes. A recent photometric study used globular clusters in NGC 1316 to constrain its star formation history, but without the knowledge of individual radial velocities. The kinematical properties of the globular cluster system in comparison with the diffuse stellar light might give more insight into the formation of NGC 1316. Of particular interest is the dark matter content. Planetary nebulae in NGC 1316 indicate a massive dark halo, and globular cluster velocities provide independent evidence.

Aims. We aim at measuring radial velocities of globular clusters in NGC 1316. We use these kinematical data to investigate the global structure of NGC 1316 and to constrain the dark matter content.

Methods. We perform multiobject spectroscopy with VLT/FORS2 and MXU. Out of 562 slits, we extract radial velocities for 177 globular clusters. Moreover, we measure radial velocities of the integrated galaxy light, using slits with a sufficiently bright sky. To these data, we add 20 cluster velocities from the literature. In an appendix, we identify new morphological features of NGC 1316 and its companion galaxy NGC 1317.

Results. The GC sample based on radial velocities confirms the colour peaks already found in our photometric study. The bright clusters, which probably have their origin in a 2 Gyr old starburst and younger star formation events, avoid the systemic velocity. A Gaussian velocity distribution is found only for clusters fainter than about $m_R = 22$ mag. The velocity distribution of clusters shows a pronounced peak at 1600 km s^{-1}. These clusters populate a wide area in the south-western region which we suspect to be a disk population. Globular clusters or subsamples of them do not show a clear rotation signal. This is different from the galaxy light, where rotation along the major axis is discernable out to 3′ radius. The kinematic major axis of NGC 1316 is misaligned by about 10° with the photometric major axis, which might indicate a triaxial symmetry. A simple spherical model like that suggested by dynamical analyses of planetary nebulae also reproduces the velocity dispersions of the faint globular clusters.

Conclusions. The central dark matter density of the present model resembles a giant elliptical galaxy. This contradicts population properties which indicate spiral galaxies as pre-merger components. Modified Newtonian dynamics (MOND) would provide a solution, but the kinematical complexity of NGC 1316 does not allow a really firm conclusion. However, NGC 1316 might anyway be a problem for a cold dark matter scenario, if the high dark matter density in the inner region is confirmed in future studies.

Key words. galaxies: individual: NGC 1316 – galaxies: kinematics and dynamics – galaxies: star clusters: general

1. Introduction

Globular clusters are "guides to galaxies" (Richtler & Larsen 2009). The photometric and kinematic properties of a globular cluster system (GCS) permit us to identify subpopulations, to constrain scenarios of galaxy formation and star formation history, and to discover the existence and shape of dark matter halos at large galactocentric radii (see Brodie & Strader 2006 and Harris 2010, for reviews). Most kinematical studies of GCSs targeted old elliptical galaxies (e.g. Strader et al. 2011; Schuberth et al. 2010; Lee et al. 2010; Romanowsky et al. 2009; Lee et al. 2008; Schuberth et al. 2006; Richtler et al. 2004 and references therein) whose GCSs show the typical bimodality of blue and red clusters which also corresponds to different kinematical properties (e.g. Schuberth et al. 2010). The red (bona fide metal-rich) clusters might have been formed in the starburst which formed the main body of elliptical galaxies, while the blue (bona fide metal-poor) population might have been donated mainly by the infall of dwarf galaxies (see Richtler 2013 for an overview). The rich GCSs of giant ellipticals, which are dominated by the metal-poor cluster populations, have probably been shaped by secular evolution rather than by major merger events (van Dokkum et al. 2010; Genel et al. 2008).

The target of the present contribution is the GCS of NGC 1316 (Fornax A). This galaxy is a thoroughly investigated merger remnant in the outskirts of the Fornax cluster and has been studied in many wavelength domains from the X-ray to the radio. See Richtler et al. (2012a, hereafter Paper I) for a

⋆ Based on observations obtained with the VLT at ESO, Cerro Paranal, Chile under the programme 078.B-0856.
⋆⋆ Appendices are available in electronic form at http://www.aanda.org

Table 1. Summary of observations (ESO programme ID 78.B-0856(A)).

Field	Centre position (J 2000)		Exp. time (s)	Seeing	No. of slits	OB Id	Night	UT (start)
1	3:23:13.0	–37:07:20	2700	0.″8	82	258629	2006-Nov-15	6:49
1	3:23:13.0	–37:07:20	2700	0.″8	82	258627	2006-Nov-15	4:53
2	3:22:58.0	–37:11:40	2700	1.″2	83	258618	2006-Nov-18	6:45
2	3:22:58.0	–37:11:40	2700	1.″3	83	258616	2006-Nov-18	7:31
3	3:23:13.0	–37:18:13	2700	1.″3	70	258615	2006-Nov-16	5:04
3	3:23:13.0	–37:18:13	2700	1.″0	70	258613	2006-Nov-16	5:59
3	3:23:13.0	–37:18:13	2700	1.″3	70	258615	2006-Nov-30	6:22
4	3:22:33.0	–37:18:39	2700	1.″2	64	258630	2006-Nov-19	5:30
4	3:22:33.0	–37:18:39	2700	1.″5	64	258632	2006-Nov-19	6:20
5	3:22:32.0	–37:15:20	2700	0.″9	68	258633	2006-Nov-19	6:53
5	3:22:32.0	–37:15:20	2700	0.″9	68	258625	2006-Nov-20	4:42
6	3:22:09.0	–37:13:52	2700	0.″8	66	258622	2006-Nov-18	5:17
6	3:22:09.0	–37:13:52	2700	0.″8	66	258624	2006-Nov-18	4:21
7	3:22:20.0	–37:08:45	2700	0.″9	64	258621	2006-Nov-20	5:47
7	3:22:20.0	–37:08:45	2700	1.″2	64	258619	2006-Nov-20	7:02
8	3:22:16.0	–37:05:36	2700	0.″8	65	258610	2006-Dec-21	3:07
8	3:22:16.0	–37:05:36	2700	1.″2	65	258612	2006-Dec-21	2:10

Notes. The seeing values are those recorded by the ESO seeing monitor.

representative summary of the work done on NGC 1316. To that we add the work on planetary nebulae (PNe) by McNeil-Moylan et al. (2012) and on the mass functions of star clusters by Goudfrooij (2012).

In the Washington photometry from Paper I, the GCS of NGC 1316 appears quite different from that of a giant elliptical galaxy. The blue and red GCs of giant ellipticals show peaks with Washington colours at $C - R = 1.35$ and $C - R = 1.75$, respectively (Bassino et al. 2006).

The colour distribution of bright clusters in the bulge region shows a clear bimodality, although it has a different meaning from that in giant ellipticals. A peak at $C - R = 1.4$ marks a starburst with an age of about 2 Gyr, which is in agreement with the spectroscopic ages and abundances of three massive star clusters (Goudfrooij et al. 2001b). A bluer peak at $C - R = 1.1$ probably corresponds to a more recent starburst 0.8 Gyr ago, but spectroscopic confirmation is still pending. A small sample of 22 bright GCs in the innermost region with radial velocities already exists (Goudfrooij et al. 2001b). In this paper we present the radial velocities of 172 additional objects in a wide field. We describe the kinematics of this cluster sample and also make dynamical remarks on this complex system.

This paper is the third in a series devoted to the cluster system of NGC 1316. Richtlter et al. (2012b; Paper II) investigates the remarkable object SH2, perhaps a dwarf galaxy which recently formed a cluster population.

We adopt the distance of 17.8 Mpc quoted by Stritzinger et al. (2010) who used the four Type Ia supernovae that have appeared so far in NGC 1316. At this distance, 1″ corresponds to 86.3 pc. The heliocentric systemic velocity of NGC 1316 is 1760 km s^{-1} (Longhetti et al. 1998).

2. Observations and data reduction

2.1. Observations

The observations were performed in service mode during seven nights (period November 14 to December 21 2006) at the European Southern Observatory (ESO) Very Large Telescope (VLT) facility at Cerro Paranal, Chile (programme 078.B-0856(A), PI: Richtler). The VLT Unit Telescope 4 (Yepun) was used with the FORS2 (FOcal Reducer/low dispersion Spectrograph) instrument equipped with the Mask EXchange Unit (MXU). The standard resolution collimator used for this programme provided a field of view of 6.′8 × 6.′8.

The detector system consisted of two 4096 × 2048 red optimized CCDs with a pixel size of 15 μm. The grism 600B gave a spectral resolution of about 3 Å. The spectral coverage was dependent on the slit position on the mask. Normally, the usable coverage was about 2000 Å with limits on the red side varying between 5500 Å and 6500 Å. We exposed eight spectroscopic masks, whose preparation is described in the next section. Flat fielding was done with internal flat lamps. A He-Ar lamp was used for wavelength calibration.

The observations are summarized in Table 1.

2.2. Mask preparation

Preimaging of the eight fields (see Fig. 1) was carried out in October 2006. Each field was observed in the R filter for 60 s. The candidate selection was based on the photometry in the Washington system (Paper I). However, at the time of the mask design, only a preliminary version of the photometry was available. Cluster candidates had to fulfill the following criteria: the allowed colour range was $0.9 < C - R < 2.1$, and the candidates should exhibit a star-like appearance on the preimages to distinguish them from background galaxies. The colour interval was defined before we became aware that NGC 1316 hosts many bluer (and younger) clusters (Paper I). Moreover, we avoided objects brighter than $R = 20$ mag; only a few bright objects were included in the sample in an effort to fill the mask.

The ESO FORS Instrumental Mask Simulator (FIMS) software[1] was then used to select the positions, widths, and lengths of the slits. A slit width of 1″ was chosen because it can also tolerate slightly worse seeing conditions.

The choice of the slit lengths was determined by the fact that most targets are very faint and therefore the best strategy is to measure sky and object in the same slit. However, this severely constrains the number of observable objects per mask, especially

[1] Available from http://www.eso.org/observing/p2pp/OSS/FIMS/FIMS-tool.html

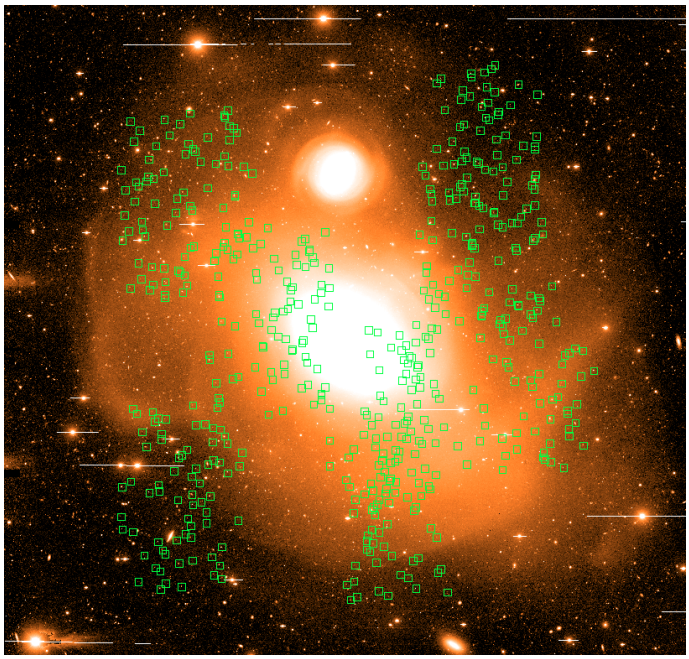

Fig. 1. Positions of the slits overlaid on a 36′ × 36′ image taken with the MOSAICII camera at the 4 m Blanco telescope, Cerro Tololo (see Paper I for more details). North is up, east to the left.

in the more crowded fields. In contrast to previous work, where we wanted to maximize the number of objects (compare Richtler et al. 2004; Schuberth et al. 2006), we now give more weight to the quality of the sky subtraction and choose relatively long slits of typically 5″. After the positioning of the slits for the selected GC candidates, the remaining space on the masks (especially in the outer fields) was used to include additional objects. Thus, some background galaxies and point sources not matching the above mentioned criteria were also observed.

2.3. The dataset

To prevent a severe contamination from cosmic ray hits, the observation of each mask was divided into two exposures of 45 min each, with the exception of Field 3 for which three science images were obtained. In all spectra, the night sky emission lines red-wards of about 5200 Å are by far the most prominent features, i.e. the spectra of the GC candidates are sky dominated. In addition to the spectroscopic observations, calibration measurements were obtained during day time. Figure 1 shows the distribution of 562 slits, located on eight FORS2 fields. Only a minor fraction of these slits finally provided radial velocities of GCs.

In total, we determined velocities for 177 GCs and 81 stars; the velocity gap between stars and GCs is sufficiently large for safe classifications. Five GCs in our sample have been already measured by Goudfrooij et al. (2001b). We found 16 quasars, and 117 galaxies. We did not attempt to derive redshifts for all objects. The remaining spectra could not be used because of low signal-to-noise ratio (S/N).

2.4. Reductions and velocity measurements

The reduction procedure and the measurement of radial velocities have already been described in numerous other papers, e.g. Schuberth et al. (2006), Richtler et al. (2004), Schuberth et al. (2010), Schuberth et al. (2012). For basic reduction, spectrum extraction, and wave-length calibration, we used the IRAF-task *identify* and *apall*.

The radial velocities were determined using the cross-correlation IRAF-task *fxcor*. Because of the very different appearance and S/N of the spectra, it turned out to be impossible to establish a standard procedure, that would always use the same task parameters. For the cross-correlation interval, we achieved good results with the range 4700 Å–5400 Å. Clearly defined correlation peaks are connected with uncertainties around 20–30 km s^{-1}. In the case of faint sources, more than one peak appeared, depending on the exact wavelength interval, within which the correlation was done. In these cases, we tried to determine which peak was the most stable against variations of the cross-correlation interval. The uncertainty then may not be the uncertainty suggested by the broadness of the correlation peak. We used as templates a high S/N spectrum of NGC 1396, obtained with the same instrumentation during an earlier run (Richtler et al. 2004) and a spectrum of one of the brightest globular clusters in NGC 4636 (Schuberth et al. 2010) (identification f12–24).

The globular cluster data are presented in Appendix B.

Table 2. Comparison of the common GCs in the sample of Goudfrooij et al. (2001b) and the present sample.

ID_G	$v_r(Goud)$	$v_r(Ri)$	ID
123	1966 ± 1	1977 ± 10	gc03384
217	1840 ± 8	1855 ± 25	gc03318
121	1627 ± 155	1618 ± 27	gc08412
204	1992 ± 19	1976 ± 34	gc02997
203	1639 ± 35	1610 ± 21	gc01324

Notes. The columns are: Identifier, velocity in Goudfrooij et al., velocity in the present paper, identifier in Tables B.1 and B.2.

2.5. Comparison with previous measurements

Because the fields were not strongly overlapping, there are only six double measurements, i.e. the same object on two different masks. In Table B.1 they are listed with the identification numbers gc01214, 2891, 2977, 3151, 4128, and 4138. The standard deviation of the velocity differences is 30 km s^{-1}. The small sample size probably prevents us from seeing more in this value than a rough approximation. However, our experience from previous work (Schuberth et al. 2010, 2012) is that the uncertainties given by *fxcor* are normally a good approximation of the true uncertainties.

Goudfrooij et al. (2001b) measured radial velocities for a small sample of GCs. Their objects are strongly concentrated in the inner regions, so that we have only five objects in common. Table 2 shows the common GCs. The zeropoints agree extremely well, leaving the velocities of Goudfrooij et al. (2001b) by only a mean of 5.4 km s^{-1} higher than our velocities. This agreement can be partly coincidental, but at least it shows that the two velocity samples do not differ greatly in their zeropoints.

Figure 2 shows the velocity uncertainties dependent on the *R*-magnitude. The uncertainties are directly taken from *fxcor*. They cluster around 50 km s^{-1} as in previous work. The three outliers with errors around 150 km s^{-1} are the objects with the photometric identification numbers (Table B.1) 341,1278, and 3025. Two of them are very faint (1278 and 3025), and the spectrum of 341 might be badly extracted.

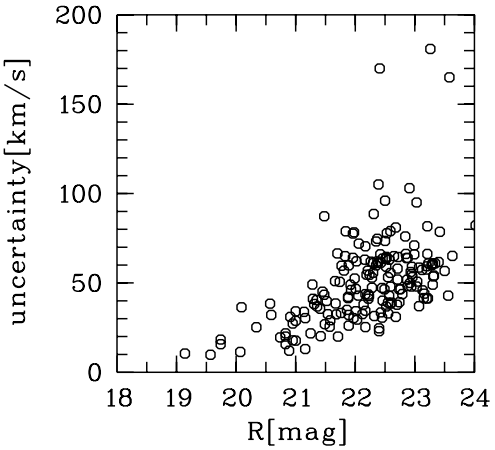

Fig. 2. Uncertainties of the radial velocities dependent on the R-magnitude.

3. Population properties and velocities

3.1. Colour–magnitude diagram and colour distribution

With the GC colours and radial velocities available from the present study, we show a clean CMD for confirmed GCs in Fig. 3 (upper panel). This CMD shows the same features found in Paper I with a larger, but contaminated photometric sample. The dashed vertical line indicates the galaxy colour as measured outside the inner dust structure (Paper I). The dotted vertical line denotes the colour ($C-R$ = 1.06) for clusters with an age of 10 Gyr and a metallicity of z = 0.0002 (Marigo et al. 2008). Clusters bluer than this must be even younger or more metal-poor; however, colour and metallicity at these low metallicity levels are not related in a simple manner (see e.g. Richtler 2013). To our sample we add 20 GCs from Goudfrooij et al. (2001b), which are coded as crosses. Their Washington colours were not been measured directly, but were transformed on the basis of Fig. 1 from Paper I using the $B-I$ colours given by Goudfrooij et al. These objects are strongly concentrated towards small radii, thus individual reddening can be an issue.

We also find some GCs distinctly bluer than $C-R$ = 1.0. These clusters cannot be old GCs. We note the outlying object at $C-R$ = 0.4, which has an age around 0.5 Gyr (metallicity is no longer a critical parameter at these blue colours). As the more complete photometry of Paper I shows, such young objects are rare, but GCs as blue as $C-R$ = 0.8 are common. If these objects have their origin in star formation events that occurred later than indicated by the peak at $C-R$ = 1.4, the assumption is reasonable that they possess at least solar metallicity. As reference values we use the ages for theoretical Washington colours for single stellar populations taken from Marigo et al. (2008) and shown in Fig. 1 in Paper I. Since we selected our spectroscopic sample with the help of our photometric data, but prior to the knowledge provided by Paper I, objects bluer than $C-R$ = 1.0 were only serendipitously targeted to fill the spectroscopic masks.

Clusters redder than the galaxy light must be metal-rich and quite old. The old metal-poor clusters, on the other hand, cannot be distinguished from younger, more metal-rich clusters, but, as argued in Paper I, there should not be too many.

The lower panel shows the corresponding colour histogram. The two peaks at $C-R$ = 1.4 and $C-R$ = 1.1 are striking and match those that have been photometrically identified. They are even weakly indicated in the small sample of Goudfrooij et al. (2001b). In Paper I we show that these peaks are only a property

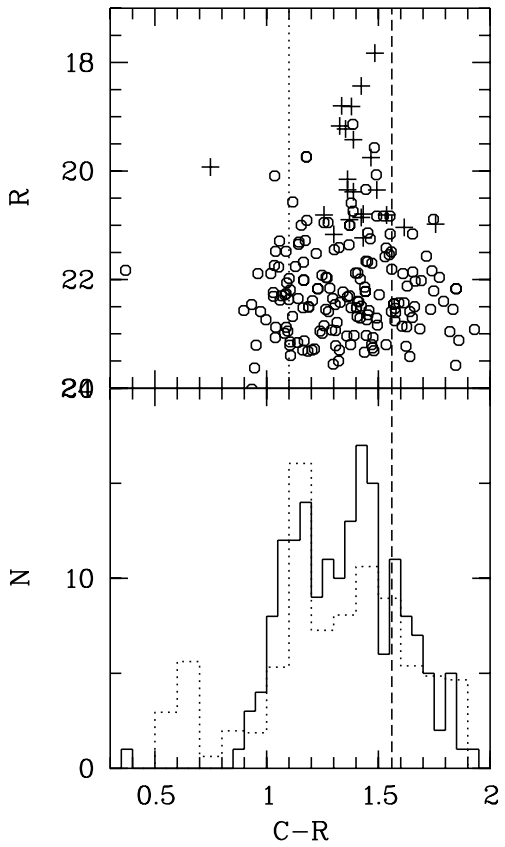

Fig. 3. *Upper panel*: CMD of confirmed globular clusters in NGC 1316 in the Washington system, marked by open circles. The photometric data are taken from Paper I. Twenty objects from Goudfrooij et al. (2001b) are denoted by crosses. The dashed vertical line denotes the galaxy colour. The dotted vertical marks the colour limit for old, metal-poor globular clusters. We also note the excess of clusters blueward of this limit which corresponds to ages of about 1 Gyr, if solar metallicity is assumed. Also note the object at $C-R$ = 0.4. *Lower panel*: corresponding colour histograms (solid histogram, only for our sample). The dotted histogram (scaled down for a convenient display) is the more complete photometric sample from Paper I. The two well-defined peaks, already indicated in Goudfrooij et al. (2001a) probably mark two epochs of high star formation rates.

of the colour distribution for bright clusters (R < 23 mag). They largely vanish if fainter clusters are also included. Paper I tentatively interprets these peaks as signatures of starbursts with ages 1.8 Gyr and 0.8 Gyr, respectively.

NGC 1316 has an interesting companion galaxy, NGC 1317 (see the appendix). Its systemic velocity is 1941 km s^{-1}. There is no indication in the photometric GC sample (Paper I) that GCs from NGC 1317 would be visible in the system of NGC1316. Moreover, the region of NGC 1317 is not covered by masks, but we cannot exclude that a few GCs belong to NGC 1317. None of the results of this contribution, however, depend on this possibility.

3.2. Velocities, colours, magnitudes

A closer look at the relation between velocities, colours, and magnitudes reveals interesting facts. In the upper panel of Fig. 4, velocities are plotted versus colours. The double peak structure in the colours is clearly discernable. A strange pattern is that the

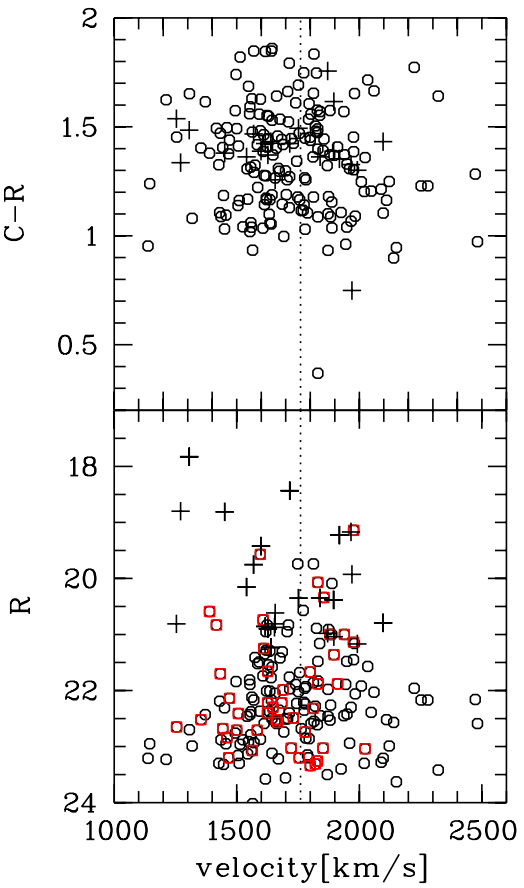

Fig. 4. *Upper panel*: velocities versus colour. Open circles denote the present GC sample, crosses the objects of Goudfrooij et al. (2001b). In both panels, the systemic velocity is marked by the dotted vertical line. The bimodal colour distribution is clearly visible. We note that the objects belonging to the peak at $C - R = 1.4$ avoid velocities higher than the systemic velocity. *Lower panel*: velocities versus R-magnitude. The brightest clusters do not show a kinematic affinity to the bulge population. We also note also the increasing velocity dispersion for clusters fainter than $R = 21.5$.

peak at $C-R = 1.4$ is populated preferably by objects with radial velocities lower than the systemic velocity.

The lower panel shows that clusters brighter than about $R = 21.5$ avoid the systemic velocity of NGC 1316. Objects with colours $1.35 < C - R < 1.5$ (the pronounced peak in Fig. 3) are marked in red. Our GCs confirm the trend, which is already visible in the sample of Goudfrooij et al., also for fainter clusters. One would expect that, if the majority of the bright clusters in red are clusters formed in the starburst with an age of about 2 Gyr (the dominant bulge population), they would also be kinematically connected to the bulge. However, the velocity field of the bulge is not known. The field stars related to the bright GC population should show the same kinematics, which does not fit at all to a Gaussian distribution around the systemic velocity. Relative radial velocities as high as 500 km s^{-1} and higher indicate that these clusters are deep in the potential well and that their orbits are elongated. Even if these objects are now projected onto the bulge, it may be that their place of birth was not the bulge, but a starburst in one of the merger components in an early stage of the merger.

The second striking observation is that the velocity distribution becomes broader with decreasing brightness. In Paper I it is shown that the bimodal colour distribution disappears if fainter clusters are included. It is therefore plausible to assume that the bright cluster population consists mainly of intermediate-age clusters belonging to a population with the complex kinematics of a merger/starburst situation still preserving, while the fainter older clusters that fill a larger volume around NGC 1316 are progressively mixed in.

3.3. Velocity histograms

The velocity histograms in several colour bins are shown in Fig. 5. The colour bins refer to the bins used in Paper I to characterize the population mix of globular clusters and which appears as a reasonable binning guided by Fig. 3. The interval $0.8 < C-R < 1.3$ contains an unknown proportion of old, metal-poor clusters and clusters younger than about 1 Gyr. The interval $1.3 < C-R < 1.6$ contains the bulk of intermediate-age clusters. In the interval $1.6 < C - R < 1.9$, one expects to find old, metal-rich clusters. Instead of a unimodal Gaussian-like distribution, one sees in all histograms, except for the reddest clusters, two velocity peaks, which are best defined for the bluer clusters. The higher velocity peak agrees well with the systemic velocity of NGC 1316, but the low velocity peak at 1600 km s^{-1} indicates a peculiarity.

The nature of this peculiarity can perhaps be inferred from Fig. 6. The objects populating the peak are preferentially located on the western side of NGC 1316, occupying a large interval of position angles. This is suggestive of a disk-like distribution of GCs seen face-on. Of course, that does not mean that the supposed disk population is present only in the interval 1550 km s^{-1}–1650 km s^{-1}. The complete dispersion in z-direction is unknown and uncertainties in the velocities widen an intrinsically sharp distribution.

3.4. Two-dimensional distribution

Figure 6 shows the two-dimensional distribution of clusters for several selections of velocities or colours/magnitudes. Because we could not achieve a complete azimuthal coverage, we have well-defined western and eastern parts. Crosses denote velocities higher than the systemic velocity of 1760 km s^{-1}, circles lower velocities. North is up, east to the left.

The upper-left panel contains the full sample. The larger symbols are objects from the HST cluster sample of Goudfrooij et al. (2001b), which populate the innermost region, where we do not find objects because of the bright galaxy light. A difference between the western and eastern part is not discernable. This changes dramatically if we select only the peak at 1600 km s^{-1}, which is the upper-right panel of the selection indicated. These objects dominantly populate the western part and it is tempting to imagine that we are looking onto a large disk or at least a structure that is thin along the line of sight. A few of these objects may belong to Schweizer's L1-structure (Schweizer 1981; Richtler 2013, see Fig. A.1), but the largest concentration is still found within the morphological bulge.

The lower panels show selections according to colour and magnitude. The left panel selects the interval $1.0 < C - R < 1.2$, which may contain younger clusters, but also old, metal-poor objects. Here we observe that most of the objects with velocities higher than the systemic velocity are located on the eastern part. The following panel selects from this sample only objects brighter than $R = 21.5$ mag. These bright clusters have a higher probability of being young (about 0.8 Gyr) than fainter objects. Practically all clusters are on the north-eastern side. The

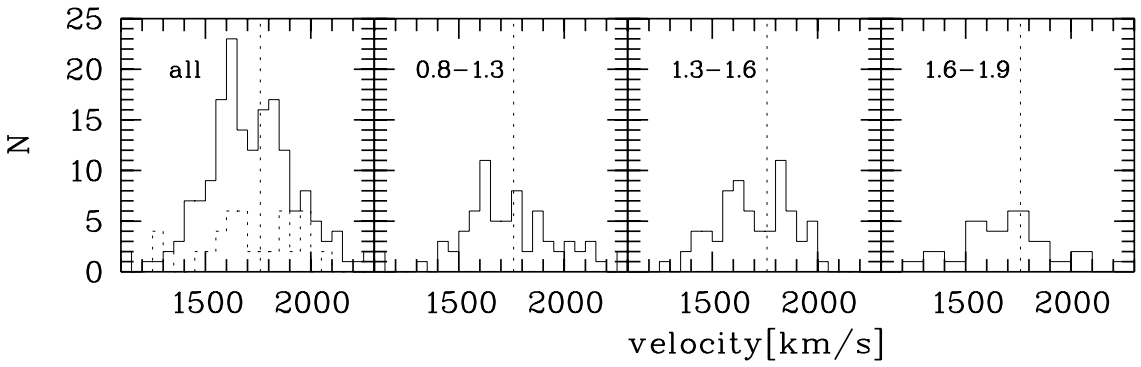

Fig. 5. Radial velocity histograms for different colour intervals, corresponding to different cluster populations (see text). Typical uncertainties are of the of order 50–80 km s^{-1} (compare Fig. 2). The vertical dotted line indicates the systemic velocity. The dotted histogram in the *left panel* is the velocity histogram of Goudfrooij et al. (2001b), where the two velocity peaks already are discernable. We interpret the peak at 1800 km s^{-1} as the expected peak at the systemic velocity. The peak at 1600 km s^{-1} is caused by a dominance of clusters with this velocity in the western part of NGC 1316.

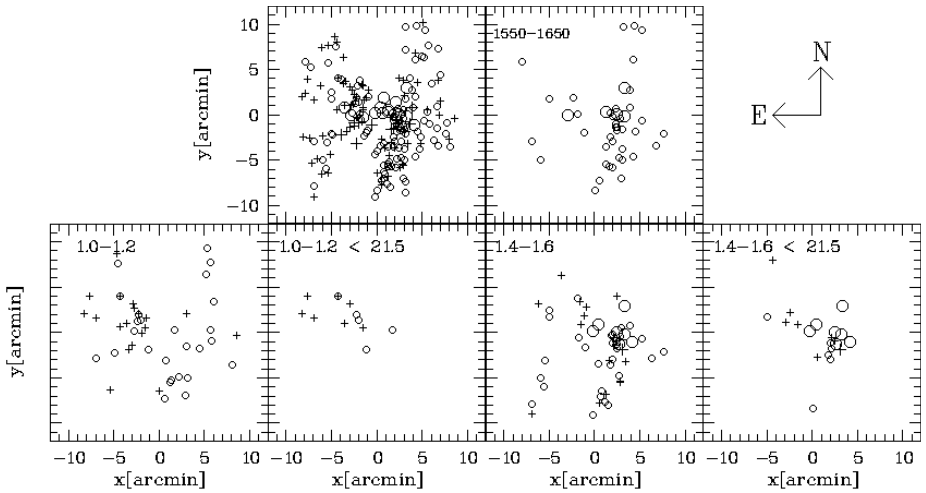

Fig. 6. Spatial distribution of globular clusters under various selections with the center of NGC 1316 as the origin. Crosses are clusters with velocities higher than the systemic velocity; open circles denote lower velocities. Large symbols are objects from the sample of Goudfrooij et al. (2001b). *Upper-left panel*: full sample, which is cleanly separated in an eastern and a western part. *Upper-right panel*: clusters with velocities between 1550 km s^{-1} and 1650 km s^{-1}. There is an overwhelming dominance of clusters on the western side of NGC 1316, indicating that these clusters intrinsically have a disk-like distribution, seen almost face-on. *Lower panels*, *from left to right*: clusters in the colour interval $1.0 < C - R < 1.2$ (blue peak); additional selection with only clusters brighter than $R = 21.5$. These are bona fide younger clusters with ages around 0.8 Gyr. Almost all are located in the north-eastern bulge region; clusters in the colour interval $1.4 < C - R < 1.6$ (red peak); additional selection with only clusters brighter than $R = 21.5$. These are bona fide younger clusters with ages around 2 Gyr and appear dominantly in the bulge region.

next panel selects $1.4 < C - R < 1.6$, an interval that hosts the brightest clusters of intermediate age. Except for the concentration at the south-western side, there is nothing striking present in the figure. Selecting only the brightest clusters (which are most likely clusters of about 2 Gyr in age), one recognizes the major axis of NGC 1316.

Bright clusters are therefore probably connected with the bulge (we have no complete knowledge about the occurrence of bright cluster at large radii), but the population is inhomogeneous regarding colour and spatial distribution.

3.5. Velocities and radial velocity dispersions

In the following we consider only our sample and disregard the objects of Goudfrooij et al. (2001b). Figure 7 shows in its upper panel the radial velocities versus the radial distance, in its lower panel the velocity dispersions in slightly overlapping bins. The bin widths of 1′ and 1.5′ have been chosen to contain about 30 objects each in order to get a statistically meaningful velocity dispersion value. The velocity dispersions have been determined using the dispersion estimator of Pryor & Meylan (1993), adopting a systemic velocity of 1760 km s^{-1}. The uncertainties have been evaluated according to the quoted maximum-likelihood formalism using the individual uncertainties of the objects. Since the bins are not independent, the error bars probably overestimate the true uncertainty. However, the physical meaning of the velocity dispersion is not interpretable in a straightforward manner. It has a well-known dynamical meaning, for example, in the case of a non-rotating spherical or elliptical system in equilibrium, while the underlying symmetry in NGC 1316 is elliptical only in the inner region. It is clear without any test for Gaussianity that the dispersions for radii larger than 5′ do not represent the dispersion of a Gaussian velocity distribution. To what extent the dominance of velocities smaller than the systemic velocity can be understood as a sample effect is difficult

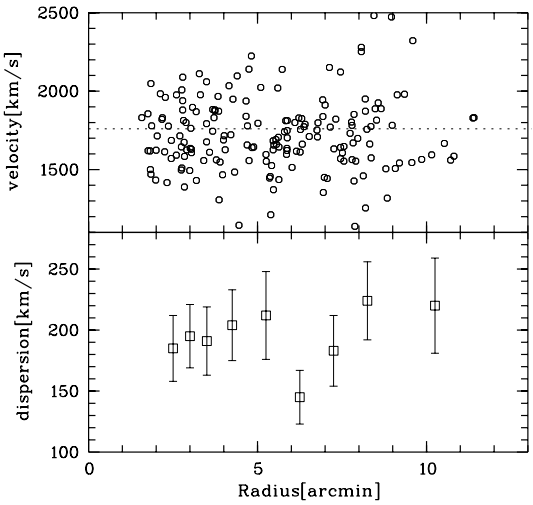

Fig. 7. *Upper panel*: radial velocities versus galactocentric distance. *Lower panel*: velocity dispersions for slightly overlapping radial bins.

to evaluate, but outside the bulge are simply more clusters in the S-W-region, and it is this region which contributes with a sharp peak at about 1600 km s^{-1}. For radii smaller than 5′ (which is the bulge), it is not so obvious. A Wilkinson-Shapiro test gives a p-value of 0.076, so the hypothesis that these objects follow a Gaussian distribution, is statistically valid, but not probable from other considerations. We come back to that shortly.

The radial increase of the dispersion probably is real, but, as Fig. 4 suggests, it may be caused by the bias towards bright clusters for smaller radii. These bright clusters show a smaller dispersion. Moreover, the relative contribution of old metal-poor clusters might be higher for larger radii, which we expect to increase the line-of-sight dispersion.

Table 3 lists the values in Fig. 7. It also lists the dispersion values for a subsample fainter than $R = 21.5$, which is more appropriate for being compared to a spherical model than the full sample (see Sect. 5), although the difference is hardly noticeable. Moreover, dispersions for an inner and an outer subsample as well as for two colour selections are given. The dispersions obviously depend in an irregular manner on the binning and sampling. The most natural assumption is that of a radially constant velocity dispersion.

3.6. Radial distribution of clusters

In Paper I we showed that the radial distribution of cluster candidates is quite different for different colour intervals. Particularly, the distribution of cluster candidates with intermediate colours does not follow a uniform power law, which means that the three-dimensionable distribution is strongly substructured.

On the other hand, we want to use the GC kinematics in the frame of a spherical model to constrain the potential. The total sample is apparently not suitable, as the kinematics of the bright clusters show. Following Fig. 4, we therefore choose all clusters fainter than $m_R = 21.5$ to define within our possibilities a sample which is the best approximation to a spherically homogeneous sample, i.e. a sample where no strong association with the inner bulge population, like the case of GC candidates of intermediate colour, is visible.

For evaluating the number density profile, we use the photometric database from Paper I (the point-source catalogue is available on-line) and select point-sources in the magnitude interval

Table 3. Velocity dispersions for different radial and magnitude/colour samples.

Radius[arcmin]	σ[km s^{-1}]	Radius[arcmin]	σ[km s^{-1}]
	no selections		$R > 21.5$
2–3	185 ± 27 (27)	2–3.5	185 ± 28 (26)
2.5–3.5	195 ± 26 (30)	3–4.5	208 ± 31 (25)
3–4	191 ± 28 (26)	4–5.5	241 ± 37 (26)
3.5–5	204 ± 28 (29)	5–6.5	199 ± 35 (32)
4.5–6	212 ± 29 (36)	6–7.5	189 ± 32 (33)
5.5–7	145 ± 22 (33)	7–8.5	236 ± 33 (28)
6.5–8	183 ± 29 (39)	–	–
7.5–9	224 ± 32 (29)	–	–
8.5–12	220 ± 39 (19)	–	–
		$1.0 < C - R < 1.2$	$1.4 < C - R < 1.6$
all	201 ± 12 (175)	182 ± 25 (45)	174 ± 26 (49)
<5	194 ± 16 (79)		
>5	206 ± 17 (96)		

Notes. Sample sizes are given in parentheses. Dispersion values for the fainter sample are used in Fig. 12.

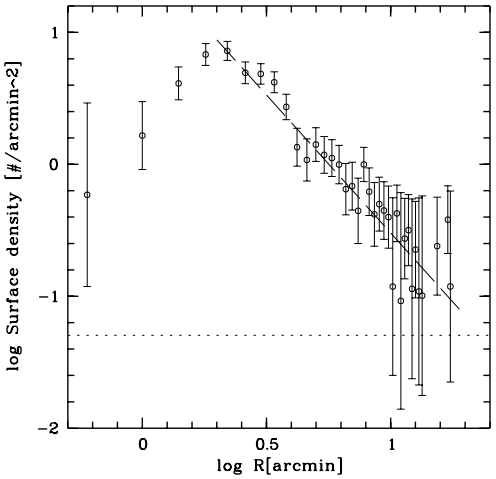

Fig. 8. Radial density profile for GC candidates fainter than $m_R = 22$ mag derived with the database in Paper I. The selection of point sources has been done as described in Paper I. The horizontal dashed line denotes the background density of GC candidates. See Eq. (1) for more details.

$22 < m_R < 24$. Figure 8 shows the resulting surface densities. The counts in the inner region become severely incomplete because of the galaxy brightness, but from 2′ outwards, the counts are fairly complete. The horizontal dotted line marks the background outside of 13′. The long-dashed line represents the beta-model

$$n(r) = 2100\left(1 + (r/r_c)^2\right)^{-1} \quad (1)$$

with $n(r)$ as the surface density in numbers/square arcmin and $r_c = 8''$ as a scale radius. Except for the factor, which has been fitted, this is the spherical model for the galaxy light from Paper I. This is a clear difference to giant elliptical galaxies, where at least the metal-poor GC subpopulation shows a shallower profile than the galaxy light. This is normally interpreted as a result of the accretion of dwarf galaxies (e.g. Richtler 2013) donating metal-poor clusters. Figure 11 in Paper I indeed shows a somewhat shallower profile for the blue clusters, but in NGC 1316 the blue clusters are a mix with unknown fractions of old, metal-poor, and younger clusters. As the intermediate clusters from Fig. 11 in Paper I demonstrate, a shallow density

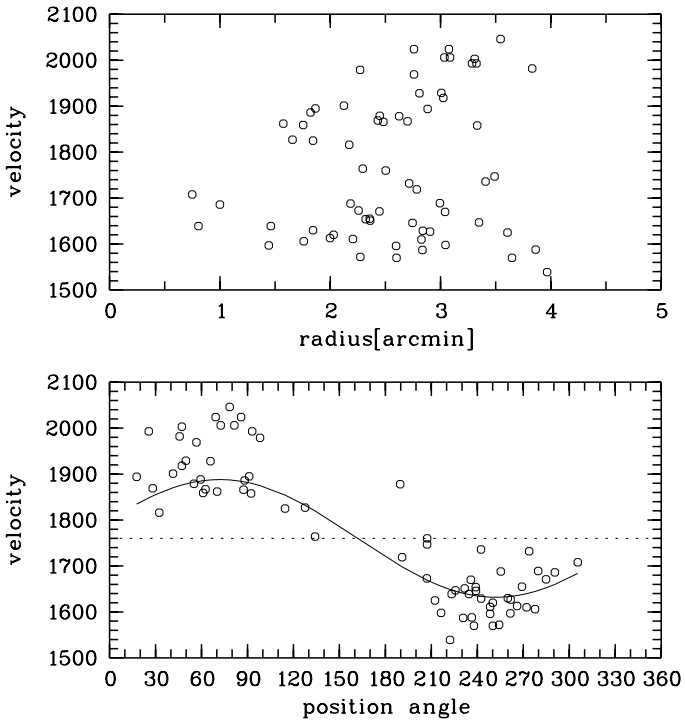

Fig. 9. *Upper panel*: radial distribution of galaxy velocities. *Lower panel*: distribution of galaxy velocities over position angles. The displayed rotation signal (represented by a sine curve) has an amplitude of 128 km s^{-1}, corresponding to the inner clusters, and peaks at 72°. The centre of rotation, indicated by the horizontal line, has the value 1760 km s^{-1}.

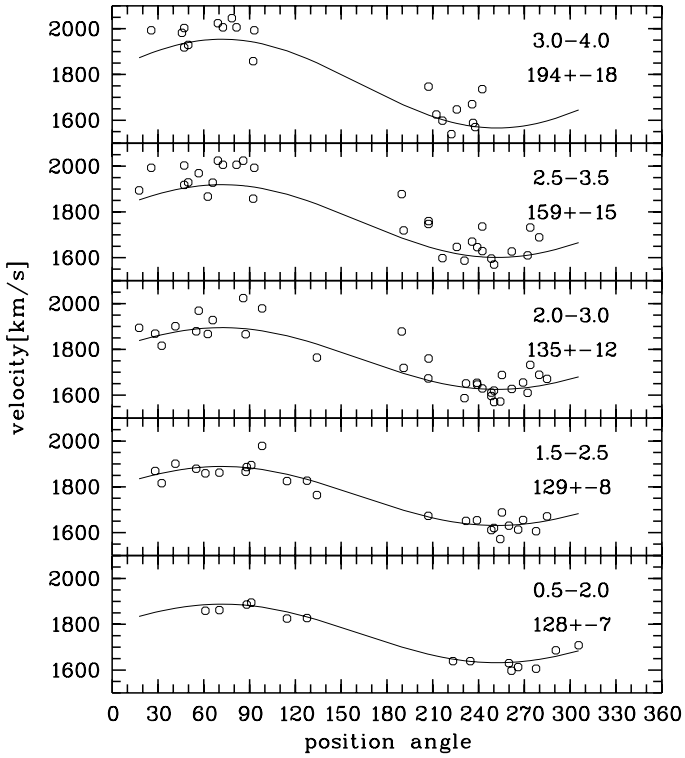

Fig. 10. Rotation signature of the galaxy light in different radial bins. The bin is indicated in arcmin, the rotation amplitude in km s^{-1}. The phase and the center of rotation has been kept at fixed values of 18° and 1760 km s^{-1}, respectively, which are excellent representations of the three inner bins. The two outer bins start to deviate to higher values, perhaps indicating a progressive deviation from a well-defined rotation.

profile is probably caused by younger clusters. The fraction of old, metal-poor objects in our faint cluster sample is unknown, but it is plausible that their number density profile is not significantly different from old, metal-rich clusters, because the pre-merger populations are expected to be well mixed dynamically.

4. Rotation of galaxy and clusters

The bulge of NGC 1316 rotates along its major axis (D'Onofrio et al. 1995; Arnaboldi et al. 1998; Bedregal et al. 2006) with an amplitude of about 100 km s^{-1}. Long-slit observations showed this rotation signal out to a radius of about 2.5′ (Bedregal et al. 2006). The kinematics of globular clusters might be related to the kinematics of the stellar population, particularly for clusters of intermediate colour which show the strongest link with the bulge (Paper I). Moreover, our data provide the possibility of enlarging the radius of measured rotation and determining the kinematical axis of the galaxy light.

4.1. Galaxy velocities and rotation signal

Some of our targets are so close to the galaxy's center that their sky spectra can be used to measure the radial velocity of the galaxy light at the location of the target. Since the masks were not designed for this purpose, we can only use slits where corresponding skyslits (now the real sky) can be found. In practice, we constructed average skyslits from regions of the mask with low background intensity and subtracted them from a given target background slit. Offsets along the dispersion direction obviously cause systematic errors, since the shape of the spectra without flux calibration depends on the position within the mask. Finally, we selected 72 slits from two masks where we measured the radial velocity by cross-correlation with NGC 1396 as the template.

Figure 9 shows the resulting velocities dependent on radius (upper panel) and position angle (lower panel). We fit the rotation signal by a sine $v_{\rm rot} = A\sin(\phi + \phi_0) + v_0$, where A is the amplitude, ϕ_0 the phase constant, and v_0 the radial velocity of the center of rotation identified with the velocity of NGC 1316. In the upper panel it is striking that the velocities higher than 1760 km s^{-1} seem to increase with radius, while the lower velocities are more or less constant. The larger velocity scatter in the two regimes of position angle do not reflect the errors, but should be real, indicating than the rotation cannot be characterized by one amplitude only. This is strengthened by the comparison with PNe. See more remarks in Sect. 6.2.

The resulting values of A for the entire sample and radial subsamples are given in Fig. 10. Since the subsamples do not differ significantly regarding the values of ϕ_0 and v_0, we fix them to $\phi_0 = 18°$, the value for the innermost sample, and $v_0 = 1760$ km s^{-1}, the systemic velocity. Thus a position angle of 72° marks the major axis of the rotation. Interestingly, this angle is larger by at least 10° than the position angle of the optical major axis, for which (Schweizer 1980) quotes a position angle of 50° at 1.0′ and 60° at 2.5′.

About 10% of the ATLAS^{3D} galaxies show this misalignment angle (Statler 1991; Krajnović et al. 2011). Out to a galactocentric distance of 2.5′ (15.5 kpc), the amplitude of the rotation signal is practically constant and very well defined. The outermost two bins are somewhat elevated, but whether this is due to an intrinsically higher rotation or due to a more complex velocity

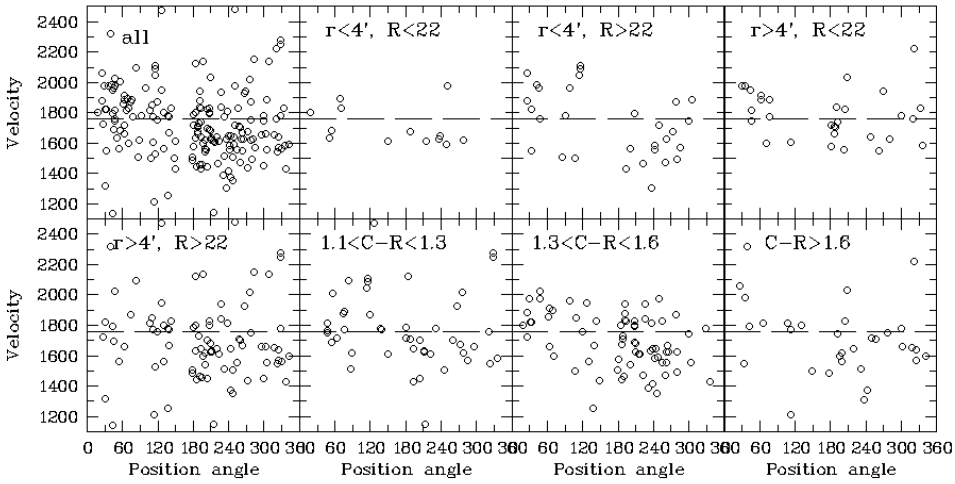

Fig. 11. Radial velocities versus position angle for different subsamples. A clear rotation signal like that of the galaxy light is nowhere visible. The sample with $r < 4'$ and $R > 22$ mag, i.e. the faint bulge clusters, seems to show the clearest rotation signal.

field, cannot be decided. The comparison with Bedregal et al. (2006) shows a very good agreement in the region of overlap.

The comparison with McNeil-Moylan et al. (2012) reveals that the amplitude of rotation of PNe in NGC 1316 is significantly smaller (85 ± 11) than our rotation amplitude of the galaxy light in the same radial regime. The PNe sample is plausibly biased towards bright PNe, stemming from younger populations, while the galaxy light samples the entire, luminosity weighted range of populations present in NGC 1316. Therefore this difference between PNe and galaxy light is suggestive of a kinematical difference between older and younger populations, as the GC kinematics reflect it.

In the projected light, the inclination of a rotating structure is not the only uncertain point. In a mix of stellar populations with different kinematic properties, some substructures may contribute to a rotation signal, others not. The rotation amplitude, as observed, may also be different at different wavelengths, if the rotational behaviour depends on the population.

4.2. Do the clusters rotate?

The comparison of the galaxy velocities with the GC velocities is interesting. The rotation signal in Fig. 10 for the innermost positions is very pure. Only for radii larger than $2'$ does one find velocities which do not fit into a strictly sinusoidal form. Part of the deviation might be caused by low S/N, but the velocities of the bright GCs suggest that there are parts of the galaxy moving with velocities strongly deviant from the systemic velocity or from a rotation pattern.

The rotation signal of the galaxy light is fundamentally different from a rotation signal of GCs. The measured velocity of the galaxy light is the luminosity-weighted mean along the line of sight without a-priori knowledge of the population that is responsible for creating a rotation signal. The GCs, on the other hand, play the role of single stars without the possibility of removing the velocity dispersion, so that one does not expect such a clear rotation as measured in the galaxy. We also expect a contaminated rotation from the fact that velocities and locations can be related, e.g. in the southern L2-structure. Figure 11 shows the radial velocities versus position angle for the entire sample and some subsamples, selected according magnitude, radius, and colour. The entire sample shows that intrinsically we find many clusters at low velocities and positions angles larger than 180°. This crowding is in part due to the objects populating the velocity peak at 1600 km s^{-1}, which seems to be related to the L1-feature of Schweizer (1980; compare Fig. A.1). The clearest rotation is seen for the sample consisting of GCs fainter than 22 mag, and closer than $4'$ to the centre. A fit to this sample reveals $a_0 = 120 \pm 64$ km s^{-1} and $\phi_0 = -1 \pm 64°$, demonstrating a large uncertainty, although it is consistent with the bulge rotation. All other GC samples do not obviously rotate.

5. Dynamical remarks

Given the kinematic complexity, including the non-negligible rotational support, the mix of GC populations and uncertain three-dimensional structure, a proper dynamical analysis is presently beyond our possibilities. However, a few remarks are adequate. The first remark to be made is that the kinematical data for the stellar population do not appear to be entirely consistent in the literature. D'Onofrio et al. (1995) measured a central velocity dispersion of 260 km s^{-1}, in good agreement with Bosma et al. (1985). The velocity dispersion then declines towards larger radii, reaching 150 km s^{-1} at $50''$, while in the Bosma et al. work, this decline is shallower and reaches 150 km s^{-1} at $80''$. Arnaboldi et al. (1998) give a central dispersion of only 200 km s^{-1} with a decline to 140 km s^{-1} at $60''$. There are also asymmetries with respect to the center, particularly pronounced along the minor axis. Bedregal et al. (2006) also find a high central dispersion of about 260 km s^{-1}, but the decline is much shallower and consistent with a constant velocity dispersion of 200 km s^{-1} between $50''$ (4.3 kpc) and $150''$ (12.9 kpc) along the major axis. Since the VLT data used by Bedregal et al. apparently have the highest S/N, we adopt in the following their kinematics. There is more agreement regarding the LOS velocities for which we adopt the Bedregal et al. values as well.

To represent the GC velocity dispersions, we avoid using the full sample because of the bright cluster kinematics, which apparently do not fit to a Gaussian. For a good sampling of the fainter clusters, we choose the limit $R > 21.5$ mag to maintain a reasonable set of statistics and bin widths of $1.5'$ with an overlap of $0.5'$. These are the open circles in Fig. 12. Looking at Fig. 7, it is not surprising that deviations from a radially constant dispersion occur. The sampling of velocities is far from ideal.

5.1. A spherical model

In spite of all shortcomings, it is interesting to present spherical models. First, it can be compared to the model of McNeil-Moylan et al. (2012), based on PNe. Second, we can

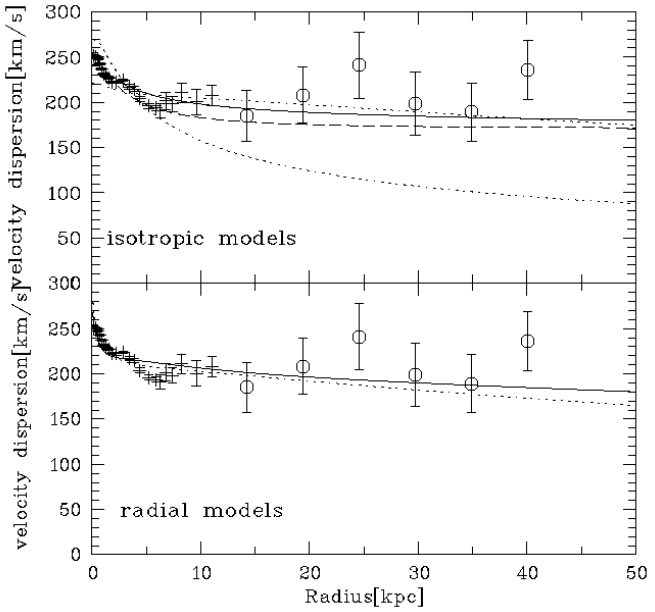

Fig. 12. In both panels the crosses mark velocity dispersions from Bedregal et al. (2006). The six open circles denote velocity dispersions of clusters fainter than $R = 21.5$ mag. *Upper panel*: some isotropic models. The lower short-dashed line is a model without dark matter and uses $M/L_R = 3.5$. The solid line is a log-halo with the parameters $v_0 = 300$ km s^{-1} and $r_0 = 0.5$ kpc and uses $M/L_R = 1.3$. The upper short-dashed line is a NFW-type halo with $M/L_R = 2.0$. See the text for its parameters. The long-dashed line is a MONDian model with $M/L_R = 2.5$. *Lower panel*: models with the radial anisotropy of Hansen & Moore (2006). The solid line is a log-halo with the same parameters as above, but with $M/L_R = 2.0$. The short dashed line is the same NFW halo as above to show that $M/L_R = 2.0$ results in a central velocity dispersion that is too high, but a stellar M/L_R lower than 2.0 is difficult to justify.

discuss the global characteristics of a dark halo without aiming at precision. Third, we can use our new photometric surface brightness profile in the R-band from Paper I. Our model uses the non-rotating spherical Jeans-equation, as do McNeil-Moylan et al. (2012). The Jeans-formalism was presented in many contributions; we refer the reader to Mamon & Łokas (2005) and Schuberth et al. (2010, 2012). The surface brightness of NGC 1316 in the spherical approximation is accurately represented by a "beta-model", which can be deprojected analytically (e.g. Schuberth et al. 2012).

We then assign an M/L-ratio (R-band) and calculate the projected velocity dispersions, adding a dark halo to the baryonic mass. We use the formulas given by Mamon & Łokas (2005). We choose a logarithmic halo (hereafter log-halo) with asymptotic circular velocity v_0 and core radius r_0, given by

$$v_{\log}(r) = v_0 r / \sqrt{r_0^2 + r^2}. \quad (2)$$

We first consider the simple case of isotropic models, which are shown in Fig. 12 (upper panel). This maximizes the stellar M/L value with respect to any radial anisotropy. To reproduce the central velocity dispersion of 250 km s^{-1} without dark matter, one needs an M/L_R value of 3.2, distinctly higher than the value of 2.5 we advocated in Paper I, and of course much higher than the value of McNeil-Moylan et al. (2012; $M/L_R \approx 1.7$), whose best-fit model is radially anisotropic. This high value has no support by any dynamical study (see the discussion in Richtler et al. 2011). Assuming solar metallicity and a Chabrier-IMF, it would correspond to an age of 5.5 Gyr as a single stellar population (Marigo et al. 2008).

To minimize the dark halo, we want to keep the stellar M/L as high as possible. On the other hand, a relatively small r_0 is needed to model the rapid decline of the stellar velocity dispersion. One has to lower M/L_R to 1.3 to permit a log-halo with $r_0 = 0.5$ kpc and $v_0 = 300$ km s^{-1}.

However, the central density of a log-halo is

$$\rho_0 = 3(v_0/r_0)^2/(4\pi G). \quad (3)$$

which means for the present halo a central density of 20 $M_\odot$/pc^3. The surface density (Donato et al. 2009) is $\rho_0 \times r_0 \approx 10^4$ $M_\odot$/pc^2. These values are not realistic in that they are much too high. Typical central densities of dark matter in massive elliptical galaxies are approximately 0.4 $M_\odot$/pc^3 (Richtler et al. 2011). We come back to that in the discussion.

For comparison, we give a MONDian halo under isotropy with the MONDian circular velocity

$$v_{\rm M} = \sqrt{v_{\rm N}^2(r)/2 + \sqrt{v_{\rm N}^4(r)/4 + v_{\rm N}^2(r) a_0 r}}, \quad (4)$$

where we adopt $a_0 = 1.35 \times 10^{-8}$ cm/s^2 (Famaey et al. 2007). Such a halo needs $M/L_R = 2.5$.

However, merger simulations indicate modest radial anisotropies. We use the findings of Hansen & Moore (2006) that the resulting anisotropy of stars in their merger simulations is related to the logarithmic slope of the three-dimensional stellar mass distribution by

$$\beta = 1 - 1.15(1 + \text{slope}(r)/6). \quad (5)$$

For our photometric model, β reaches a constant radial anisotropy of +0.4 at about 5 kpc. A good approximation for this relation is the anisotropy profile considered by Mamon & Łokas (2005), $\beta = 0.5(r/(r + r_a))$, r_a being a scale radius with any low value. Adopting this kind of anisotropy, we can conveniently apply the formalism given by Mamon & Łokas (2005). A consequence of the anisotropy is to lower the stellar M/L ratio to comply with the central velocity dispersion, which is boosted by the projected radial contributions. In the outer parts, the radial anisotropy results in a lower projected velocity dispersion. So we have to lower the M/L even more (which contradicts all existing dynamical and population evidence) or work with a more realistic value and reduce drastically the dark matter content in the inner region.

The parameters $M/L_R = 2$, $r_0 = 5$ kpc, and $v_0 = 300$ km s^{-1} do a good job. This halo is shown in Fig. 12. Its central density is 0.2 $M_\odot$/pc^3 and the surface density is 10^3 $M_\odot$/pc^2, which are consistent with values for massive elliptical galaxies. This is more or less a halo of the kind that McNeil-Moylan et al. (2012) derived from PNe.

To enable the comparison with the dark matter densities of elliptical and spirals by Napolitano et al. (2010), we also give dark matter profiles of the NFW-type,

$$\rho = \frac{\rho_{\rm s}}{r/r_{\rm s}(1 + r/r_{\rm s})^2} \quad (6)$$

with $\rho_{\rm s}$ and $r_{\rm s}$ being a characteristic density and a scale radius, respectively. With $r_{\rm s} = 17$ kpc and $\rho_{\rm s} = 0.028$ $M_\odot$/pc^3 in combination with $M/L_R = 2.0$, one has a good representation in the isotropic case (Fig. 12, upper panel). For the anisotropic case (lower panel), we use the same parameters to show that the central velocity dispersion becomes too high and the M/L-value

has to be lowered. The mean density within an effective radius of 68.9″ (Paper I, appendix) or 6 kpc is 0.079 $M_{\odot}/\mathrm{pc}^3$. Comparing this value with Fig. 9 of Napolitano et al. (2010) shows that it is a typical value for a massive elliptical. We comment on this later in the discussion.

Looking at other halo shapes is not worthwhile, given the observational constraints and model restrictions. They will differ in details, but not in the main conclusions which we reserve for the discussion (see Sect. 6.3).

6. Discussion

6.1. The GC colour distribution within the globular cluster system

It is very satisfactory that in the colour distribution of the pure GC sample, the same features appear as in the photometric sample, namely a peak at $C-R \approx 1.4$ and a peak at $C-R \approx 1.1$. This bimodal appearance of the colour distribution in NGC 1316 has little to do with the bimodality, which is found in the GCSs of giant ellipticals, where the blue peak ($C-R \approx 1.3$) consists of metal-poor, probably accreted clusters and the red peak of metal-rich clusters ($C-R \approx 1.7$) formed with the majority of the metal-rich field population of the host galaxy (e.g. Richtler 2013). Although ages have been spectroscopically determined only for a few of the brightest clusters (Goudfrooij et al. 2001b) of the red peak, clusters as young as 0.5 Gyr can be identified by photometry alone, provided that a radial velocity is available which excludes the nature as a background galaxy or as foreground star. The detections of GCs bluer than $C-R = 1.0$ are serendipitous and more objects remain to be discovered. The colour interval between the red peak and $C-R \approx 1.0$ could be populated by metal-poor, old clusters, but since clusters around 0.5 Gyr definitely exist, we would also expect clusters with ages between 2 Gyr (the red peak) and 0.5 Gyr. The colour variation among the brightest clusters might indicate the duration of a period with a high star formation rate, but high S/N spectra are necessary to investigate this in more detail, as well as to find out the fraction of old, metal-poor clusters. One notes the absence of very bright clusters in the blue peak, but we designed our masks leaving out objects brighter than $R = 20$ mag and bluer than $C-R \approx 1.0$ (because we did not expect such bright and blue objects).

6.2. Comparison with planetary nebulae

Although it is beyond our scope to discuss in detail the kinematics of PNe presented by McNeil-Moylan et al. (2012), some remarks on the comparison between GCs and PNe are appropriate. The question is to what level are the kinematic properties of PNe and GCs comparable? The youngest GC populations will have no PN counterparts and the main population of bright PNe will stem from intermediate-age populations (Buzzoni et al. 2006). The velocity dispersions of the total samples of GCs and PNe agree within the uncertainties.

Figure 13 shows velocity distributions of PNe, using the list published by McNeil-Moylan et al. (2012). The upper-left panel shows the total sample, which is also presented by McNeil-Moylan et al., but here the binning is different and the peak near the systemic velocity of NGC 1317 is not visible. The PNe inside a radius of 2.5′ (lower-left panel) show a picture similar to the bright inner GCs. We cannot compare with the GC population within the same radius, but the comparison with GCs within 5′ (needed to produce comparable numbers), shows a perplexing agreement. The GCs are depicted by the

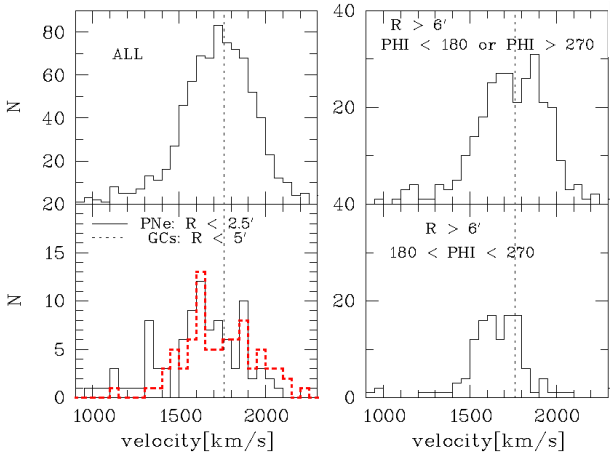

Fig. 13. For comparison with the GCs, some PNe samples are shown. *Upper-left panel*: entire sample for comparison. *Lower-left panel*: inner PNe (solid line). We note the striking similarity with the globular clusters (dashed red line). *Upper-right panel*: outer PNe covering a position angle interval of 270° with the exception of the south-western quadrant. Here the velocity distribution is symmetric with respect to the systemic velocity. This histogram is meant as a supplement to the lower-right panel. *Lower-right panel*: the south-western quadrant. As in the case of globular clusters (Fig. 5), the velocity distribution is shifted towards lower velocities. The peak at 1600 km s^{-1} is not as pronounced as in the case of globular clusters.

dashed histogram. The peaks at 1600 km s^{-1} and 1900 km s^{-1} are exactly reproduced. This agreement vanishes when PNe at larger radii are included. Because of the galaxy's brightness in the central parts, one may assume that the PNe are particularly bright and that most of them belong to the 2 Gyr population. We interpreted the velocity peak of GCs at 1600 km s^{-1} as a signature of a disk-like distribution of clusters in the outer south-western part of NGC 1316, which is dominated by Schweizer's L1 structure. This view still holds, when looking at the lower-right panel of Fig. 13, which is the outer south-western quadrant of the PNe distribution. The shift of the distribution and the peak at 1600 km s^{-1} are clearly visible. The upper-right panel for comparison shows the complementary distribution which is well centered on the systemic velocity, but then one would not expect that the inner peak at about the same velocity to be due to the same feature, unless there is a disk-like distribution of PNe over the entire galaxy. This issue remains open for further investigation.

Another interesting point emerges from the comparison of Fig. 9 with the distribution of PNe velocities. Figure 9 shows that the galaxy velocities reach quite high values for the largest distances and position angles in the range between 0° and 90°. The same can be seen in the PNe velocity distribution. The highest PNe velocities are found in the radial distance range $2.9' < R < 4.3'$. If we select PNe with these distances, we can plot Fig. 14 which shows velocities versus position angles. The PNe population between 0° and 90° is striking. It represents the stellar population in the lines-of-sight along which the galaxy velocities are measured. Since the galaxy velocities are luminosity-weighted mean values, their nature is difficult to analyse without the knowledge of the full velocity field, but velocities as high as 2200 km s^{-1} are hardly rotation velocities and are probably related to the merger history.

The velocity distribution of GCs in the bulge region is very similar to the velocity distribution of PNe, but at larger radii the velocity dispersions differ significantly. The velocity dispersion

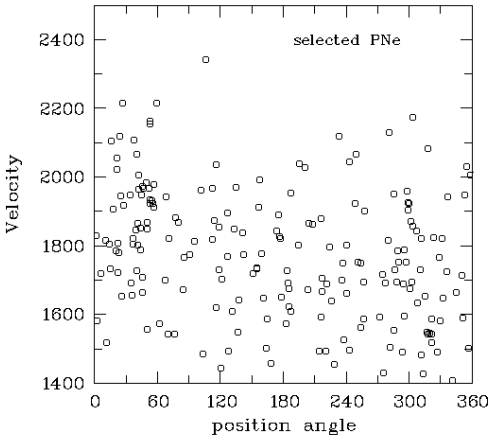

Fig. 14. Selection of the PNe from McNeil-Moylan et al. (2012): distance between 2.9′ and 4.3′. This plot is similar to Fig. 9 in that there is a striking population of high PNe velocities at position angles of less than 60°. The velocity distribution of PNe might represent the velocity distribution along the line-of-sight, which is measured with luminosity weights by the integrated light.

of GCs is more or less constant, while that of the PNe starts to decline at a radius of 200″ (about 17.3 kpc). Since both trace the same mass, any difference is probably due to a difference in the three-dimensional distribution. Again, any reasoning must remain speculative at this point because of the uncertainty regarding this distribution and the detailed population properties. The parent population of PNe is of intermediate age, while GCs cover a larger range of ages. Even if we cannot identify old clusters, one would reasonably assume their presence. Their spatial distribution will be more spherical than that of the PNe, which trace the outer stellar structures. The GC sample at larger radii will also contain a higher proportion of old clusters compared to the bulge population. We therefore suspect that the PNe will contain a higher fraction of objects belonging to a somewhat flattened parent population, which in a radial average naturally results in a lower line-of-sight dispersion.

6.2.1. High velocity offsets

In the GC sample and even more in the PNe sample, one finds a few objects with astonishingly large radial velocity offsets to NGC 1316, especially in the case of PNe up to 1000 km s^{-1}. As McNeil-Moylan et al. (2012) suggest, some of the extreme cases may be Lyman-α galaxies at $z = 3$.

In the Milky Way, such velocities would be called hypervelocities and a common interpretation is the acceleration by the supermassive black hole (SMBH) in the galactic center (e.g. Brown et al. 2012; Hills 1988). These objects are extremely rare. The SMBH in NGC 1316 is more massive and the stellar density might be higher, but one would not expect to find these stars in appreciable numbers in a PNe sample (in this case, the kinematics of PNe would perhaps not say much about the potential of NGC 1316). Large velocity offsets have also been found in NGC 1399 (Richtler et al. 2004; Schuberth et al. 2010), but NGC 1399 is in the center of the Fornax cluster, while there are no such large potential differences near NGC 1316. The other possibility is that radial velocities near 1000 km s^{-1} are recession velocities rather than peculiar velocities. The PNe would then belong to an intergalactic population. This has been suspected before in the case of GCs around NGC 1399 (Richtler et al. 2003), but until now could be neither confirmed nor discarded.

6.3. The dark halo of NGC 1316: Spiral galaxy or elliptical galaxy?

As discussed in Paper I, all evidence points toward spiral galaxies as pre-merger components. In brief, the arguments are that the old globular cluster system, although it cannot be identified cluster-by-cluster, must be quite poor, not fitting to a giant elliptical galaxy. Moreover, a simple population synthesis requires an intermediate-age population for the pre-mergers in order to reproduce the galaxy colour, not an old population. On the other hand, the dark halo *does not show the characteristics of dark halos of spiral galaxies, but fits to massive elliptical galaxies.*

As first shown by Gerhard et al. (2001), the dark halos of spiral galaxies, when represented by logarithmic halos, have central densities significantly lower than those of elliptical galaxies of comparable mass. The estimated factors vary between 10 and 30. These factors appear to be lower in the more recent work of Napolitano et al. (2010). However, the central density of our low-density log-halo (0.2 $M_\odot$/pc^3) is what we would expect for an elliptical galaxy with a stellar mass of about 2.5×10^{11} $M_\odot$. The dark halo of McNeil-Moylan et al. (2012) has a central density of 0.12 $M_\odot$/pc^3, but their model has a constant radial anisotropy of $\beta = +0.4$ and demands $M/L_B = 2.8$ which corresponds to about $M/L_R = 1.7$, quite a low value, which would correspond to a single stellar population of 1 Gyr (Marigo et al. 2008). As the authors say, these parameters may change with a more sophisticated modeling. However, one would expect that the collisionless merging of two dark matter halos would *lower* the characteristic densities and not enhance them. It is perhaps too early to call this a serious problem in view of the simplicity of the present approach. At least it points toward the possible existence of an inconsistency in the context of ΛCDM and adds to the many other unsatisfactory findings. For a deeper discussion see the reviews of Kroupa (2012) and Famaey & McGaugh (2012).

That the MONDian interpretation with $M/L_R = 2.5$ works quite well, is at least remarkable. Again, it is not necessarily a strong point for MOND, given the equilibrium assumption of an apparently quite chaotic system. However, NGC 1316 would not be the first galaxy outside the world of disk galaxies, where MOND works well only with an M/L, which fits to their evolutionary history. Milgrom (2012) recently showed, that the isolated ellipticals NGC 720 and 1521 are consistent with the MONDian phenomonology. Both are late merger remnants (as is the case with many isolated ellipticals; Tal et al. 2009; Lane et al. 2013) with lower M/L-values than for old, metal-rich elliptical galaxies. So it not only seems that the MONDian phenomenology extends to elliptical galaxies (or in other words, that elliptical galaxies fall onto the same baryonic Tully-Fisher relation as disk galaxies), but also that from the ΛCDM point of view, the dark matter content depends somehow on the M/L values of the stellar population, which would be intriguing.

7. Summary and conclusions

We present radial velocities of 177 globular clusters in NGC 1316 (Fornax A), obtained with mask spectroscopy using FORS2/MXU at the VLT. To these data, we add 20 radial velocities from Goudfrooij et al. (2001b). Moreover, we determined radial velocities for the galaxy background light at 68 locations out to a radius of 4′. We discuss the kinematical structure of the globular cluster system and use existing data in combination with the globular clusters to present a spherical dynamical model, using the photometric model from Paper I.

The most important findings are:

- The colour distribution of confirmed GCs is bimodal, showing the same peaks as in the larger, but contaminated photometric sample of GCs. To these peaks, we assign two epochs of particularly high star formation rate, one at 2 Gyr and one at 0.8 Gyr. Moreover, we confirm that there are a few clusters as young as 0.4 Gyr.
- Globular clusters brighter than about $M_R \approx -10$ mag avoid the systemic velocity, particularly so the bright clusters of the Goudfrooij et al. sample, which are constrained to the inner 5 kpc. Their field stellar counterpart might be an extended stream. In this case, one would expect many more bright clusters at large distances. The inner planetary nebulae show a stunningly similar pattern.
- A striking peak in the velocity distribution at 1600 km s^{-1} is mainly populated by clusters outside the bulge in the south-western region of NGC 1316. This peak may indicate a disk-like distribution of star clusters. We suggest that they belong to the structure L1, which is a bona fide remnant of an infalling dwarf galaxy.
- The velocity dispersion of GCs shows a clear dependence on cluster brightness by getting higher for fainter clusters, reaching a value of about 200 km s^{-1}.
- Out to 3′, the galaxy light shows a clear rotation signal with a more or less constant amplitude of about 130 km s^{-1}. We do not find any subpopulation of GCs with a similarly clear rotation. At larger radii the velocities scatter significantly, but we cannot distinguish between a chaotic velocity field and large errors due to low S/N-spectra.
- Disregarding the question, whether spherical models are good approximations or not, we present logarithmic halos as the dark matter halos, which can reproduce quite well the kinematics of the stellar light and the globular clusters. Valid parameters are $r_0 = 5$ kpc, $v_0 = 320$ km s^{-1}, corresponding to a central dark matter density of around 0.2 $M_\odot$/pc^3. This halo is quite similar to the dark halo shown by McNeil-Moylan et al. (2012).

Given the entire kinematic evidence, the GCS cannot be described by simple morphological parameters as is the case with many giant ellipticals. The large variety of ages (metallicities are unknown), the uncertain three-dimensional arrangement, and the perhaps complex velocity field reflect the complex history of kinematics and dynamics.

The present dark halo shows high dark matter densities typical of a massive elliptical galaxy, although all indications instead point to spirals as merger progenitors. After merging activity, one would expect the pre-merger dark matter densities to be even lower. This conflict is perhaps resolvable with MOND. Whatever the truth, NGC 1316 and its dark matter halo is probably a crucial object in the discussion of ΛCDM and alternate gravity theories.

Acknowledgements. We thank the anonymous referee for valuable and helpful comments. T.R. acknowledges financial support from FONDECYT project No. 1100620, and from the BASAL Centro de Astrofísica y Tecnologias Afines (CATA) PFB-06/2007. T.R. also thanks ESO/Garching, where the revised version was completed. M.G. thanks UNAB/DGID for financial support. L.P.B. acknowledges support by grants from Consejo Nacional de Investigaciones Científicas y Técnicas and Universidad Nacional de La Plata (Argentina).

References

Arnaboldi, M., Freeman, K. C., Gerhard, O., et al. 1998, ApJ, 507, 759
Bassino, L. P., Richtler, T., & Dirsch, B. 2006, MNRAS, 367, 156
Bedregal, A. G., Aragón-Salamanca, A., Merrifield, M. R., & Milvang-Jensen, B. 2006, MNRAS, 371, 1912
Bosma, A., Smith, R. M., & Wellington, K. J. 1985, MNRAS, 212, 301
Brodie, J. P., & Strader, J. 2006, ARA&A, 44, 193
Brown, W. R., Geller, M. J., & Kenyon, S. J. 2012, ApJ, 751, 55
Buzzoni, A., Arnaboldi, M., & Corradi, R. L. M. 2006, MNRAS, 368, 877
Donato, F., Gentile, G., Salucci, P., et al. 2009, MNRAS, 397, 1169
D'Onofrio, M., Zaggia, S. R., Longo, G., Caon, N., & Capaccioli, M. 1995, A&A, 296, 319
Famaey, B., & McGaugh, S. S. 2012, Liv. Rev. Relat., 15, 10
Famaey, B., Gentile, G., Bruneton, J.-P., & Zhao, H. 2007, Phys. Rev. D, 75, 063002
Genel, S., Genzel, R., Bouché, N., et al. 2008, ApJ, 688, 789
Gerhard, O., Kronawitter, A., Saglia, R. P., & Bender, R. 2001, AJ, 121, 1936
Goudfrooij, P. 2012, ApJ, 750, 140
Goudfrooij, P., Alonso, M. V., Maraston, C., & Minniti, D. 2001a, MNRAS, 328, 237
Goudfrooij, P., Mack, J., Kissler-Patig, M., Meylan, G., & Minniti, D. 2001b, MNRAS, 322, 643
Hansen, S. H., & Moore, B. 2006, New Astron., 11, 333
Harris, W. E. 2010, Roy. Soc. Lond. Phil. Trans. Ser. A, 368, 889
Hills, J. G. 1988, Nature, 331, 687
Horellou, C., Black, J. H., van Gorkom, J. H., et al. 2001, A&A, 376, 837
Krajnović, D., Emsellem, E., Cappellari, M., et al. 2011, MNRAS, 414, 2923
Kroupa, P. 2012, PASA, 29, 395
Lane, R. R., Salinas, R., & Richtler, T. 2013, A&A, 549, A148
Laurikainen, E., Salo, H., Buta, R., et al. 2006, AJ, 132, 2634
Lee, M. G., Hwang, H. S., Park, H. S., et al. 2008, ApJ, 674, 857
Lee, M. G., Park, H. S., Hwang, H. S., et al. 2010, ApJ, 709, 1083
Lin, L.-H., Yuan, C., & Buta, R. 2008, ApJ, 684, 1048
Longhetti, M., Rampazzo, R., Bressan, A., & Chiosi, C. 1998, A&AS, 130, 267
Mackie, G., & Fabbiano, G. 1998, AJ, 115, 514
Mamon, G. A., & Łokas, E. L. 2005, MNRAS, 363, 705
Marcum, P. M., O'Connell, R. W., Fanelli, M. N., et al. 2001, ApJS, 132, 129
Marigo, P., Girardi, L., Bressan, A., et al. 2008, A&A, 482, 883
McNeil-Moylan, E. K., Freeman, K. C., Arnaboldi, M., & Gerhard, O. E. 2012, A&A, 539, A11
Milgrom, M. 2012, Phys. Rev. Lett., 109, 131101
Napolitano, N. R., Romanowsky, A. J., & Tortora, C. 2010, MNRAS, 405, 2351
Papovich, C., Giavalisco, M., Dickinson, M., Conselice, C. J., & Ferguson, H. C. 2003, ApJ, 598, 827
Piner, B. G., Stone, J. M., & Teuben, P. J. 1995, ApJ, 449, 508
Pryor, C., & Meylan, G. 1993, in Structure and Dynamics of Globular Clusters, eds. S. G. Djorgovski, & G. Meylan, ASP Conf. Ser., 50, 357
Richtler, T. 2013, in 370 Years of Astronomy in Utrecht, eds. G. Pugliese, A. de Koter, & M. Wijburg, ASP Conf. Ser., 470, 327
Richtler, T., & Larsen, S. 2009, Globular Clusters – Guides to Galaxies, Proc. of the Joint ESO-FONDAP Workshop on Globular Clusters (Springer)
Richtler, T., Dirsch, B., & Geisler, D. 2003, in Extragalactic Globular Cluster Systems, ed. M. Kissler-Patig, 293
Richtler, T., Dirsch, B., Gebhardt, K., et al. 2004, AJ, 127, 2094
Richtler, T., Famaey, B., Gentile, G., & Schuberth, Y. 2011, A&A, 531, A100
Richtler, T., Bassino, L. P., Dirsch, B., & Kumar, B. 2012a, A&A, 543, A131 (Paper I)
Richtler, T., Kumar, B., Bassino, L. P., Dirsch, B., & Romanowsky, A. J. 2012b, A&A, 543, L7 (Paper II)
Romanowsky, A. J., Strader, J., Spitler, L. R., et al. 2009, AJ, 137, 4956
Sanderson, R. E., & Helmi, A. 2013, MNRAS, 435, 378
Schuberth, Y., Richtler, T., Dirsch, B., et al. 2006, A&A, 459, 391
Schuberth, Y., Richtler, T., Hilker, M., et al. 2010, A&A, 513, A52
Schuberth, Y., Richtler, T., Hilker, M., et al. 2012, A&A, 544, A115
Schweizer, F. 1980, ApJ, 237, 303
Schweizer, F. 1981, ApJ, 246, 722
Statler, T. S. 1991, AJ, 102, 882
Strader, J., Romanowsky, A. J., Brodie, J. P., et al. 2011, ApJS, 197, 33
Stritzinger, M., Burns, C. R., Phillips, M. M., et al. 2010, AJ, 140, 2036
Struck, C., Dobbs, C. L., & Hwang, J.-S. 2011, MNRAS, 414, 2498
Tal, T., van Dokkum, P. G., Nelan, J., & Bezanson, R. 2009, AJ, 138, 1417
van Dokkum, P. G., Whitaker, K. E., Brammer, G., et al. 2010, ApJ, 709, 1018

Pages 14 to 18 are available in the electronic edition of the journal at http://www.aanda.org

Appendix A: Morphological remnants of dwarf galaxies

We supplement our morphological remarks of Paper I by calling attention to structures that have either not been noted or that have been mentioned with an unclear interpretation. In the following, we use the designations of Schweizer (1980, see Fig. A.1: L = loop, R = ripple, P = plume). Additionally, we introduce O1 as "object 1".

Already Mackie & Fabbiano (1998) showed residuals from an elliptical model, based on a photographic B-plate. Here we see in more detail the complex structures which become visible after the subtraction of the elliptical model from Paper I. Figure A.1 shows the wide field, while Fig. A.2 demonstrates the structure in the inner parts. The shell system was first described by Schweizer (1980). He identified two ripples on the south-western part, we see at least four. Striking is the L2-structure in its full extension. In the epoch of Schweizer's paper, computer simulations of galaxy interactions were just at their very beginning. Today we identify L2 as the long tidal tail of an infalling dwarf galaxy. Morphologically, it might be connected either to NGC 1317 or to Schweizer's ripple R2, which Schweizer suggested, but if NGC 1317 were related to this tidal structure, we would not expect such a seemingly undisturbed spiral structure. The physical link to R2 is also doubtful, given the quite different widths of the structures in the area of overlap.

Shells appear in simulations as caustics in phase space after the infall of a dwarf galaxy on a radial orbit into the potential of a larger galaxy (e.g. Sanderson & Helmi 2013). A morphological characteristic of these caustics are the sharp outer boundaries which are the turn-around points of stellar orbits. Indeed, we find these sharp boundaries in NGC 1316 at the well-known southern L1-feature, which accordingly has to be interpreted as the remnant of a smaller galaxy, but we also find them at some locations in the shell system, most strikingly in the region of the plume. It is difficult to see how *radial* orbits can play a role in this case. It might be of significance that the plume itself (which is probably an infalling dwarf given its population properties, see Paper I) has a radial structure.

The ripples are suprisingly coherent. Following the outer shell clockwise, starting at the plume position, one is led on a spiral-like pattern to the inner region. Interestingly, this path avoids the ripple R2.

Another pattern, which occurs in simulations (e.g. Sanderson & Helmi 2013), are the T-like features. One conspicious example is located between L2 and L4.

Besides the plume region, the brightest residual is found at 50″ west, 90″ south, labelled "O1". Figure A.3 shows the region of this object. It is striking that O1 exhibits a larger density of sources than are found in its environment.

A.1. NGC 1317

To our knowledge the companion galaxy had never been the topic of a dedicated publication, although many highly interesting features can be identified. Morphological and stellar population aspects have been discussed by e.g. Schweizer (1980), Marcum et al. (2001), Papovich et al. (2003) and particularly by Laurikainen et al. (2006), who used near-infrared filters. Here we briefly add a few morphological remarks on NGC 1317 on the basis of a colour map, as has been done for NGC 1316 in Paper I, and HST-images, which to our knowledge have not yet been shown in the literature. NGC 1317 is a double-barred spiral galaxy with star formation occurring within a ring-like area. In

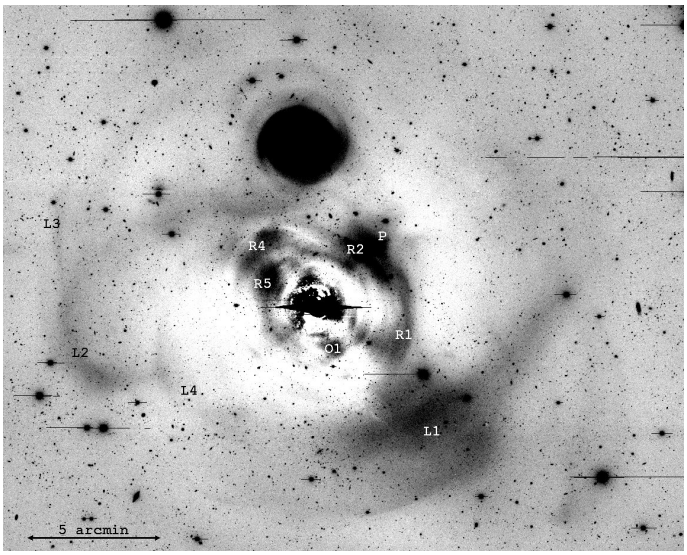

Fig. A.1. Residuals in *R* after subtraction of a smooth elliptical model. North is up, east to the left. The designations are from Schweizer (1980). This global view shows Schweizer's L2 structure as a tidal tail.

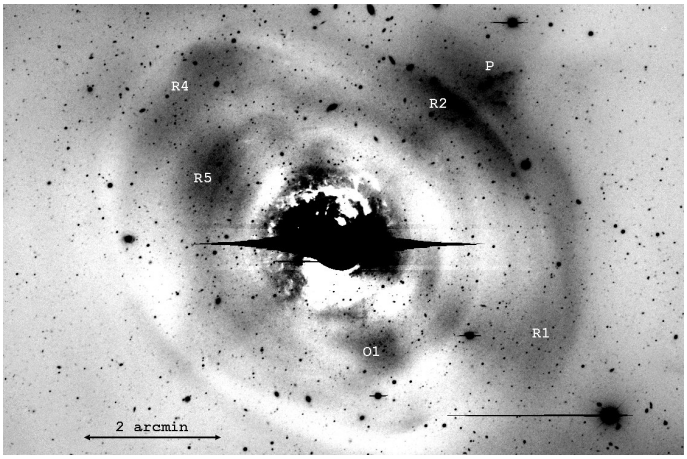

Fig. A.2. Residuals in *R* of the inner part. The dynamical range is chosen to make the shells better visible. We note particularly the sharp boundary of the shell R2.

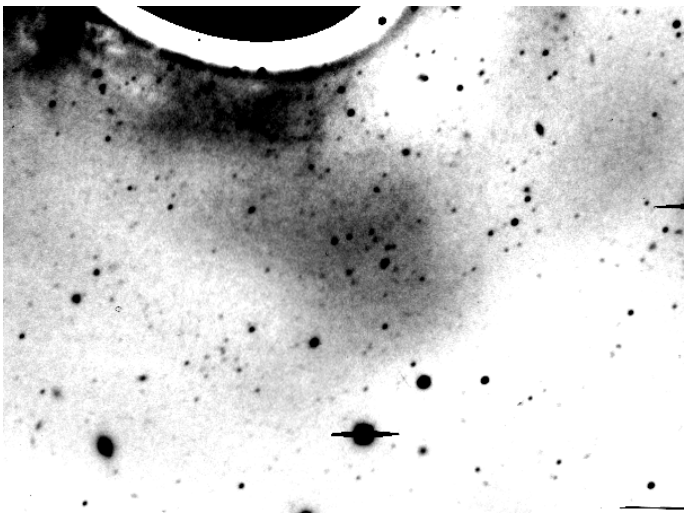

Fig. A.3. Amplified region around O1. We note the apparently larger number of sources projected onto O1, which may be star clusters. One may speculate that O1 is the remnant of a dwarf galaxy.

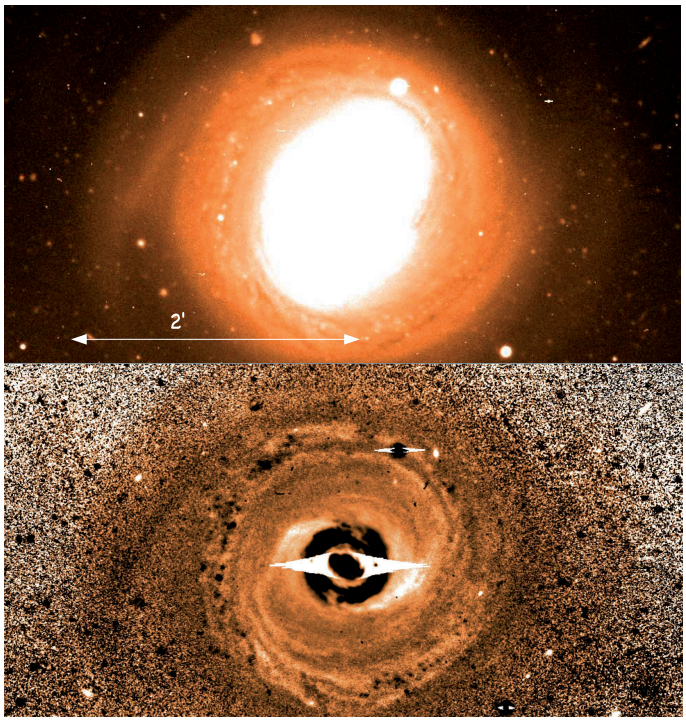

Fig. A.4. *Upper panel*: our C-image of NGC 1317, where because of the higher extinction the dust features are much more visible than in the R-image. North is up, east to the left. The scale is valid for both panels. *Lower panel:* colour map using Washington C and Harris R (Paper I). The dynamical range of the colour wedge is $1.3 < C - R < 2$. Blue is dark, red is bright. We note the inner star forming ring, which appears black. The bright features denote dust patterns. Outside the ring, additional young populations are visible as black spots arranged in a ring-like fashion on the eastern side.

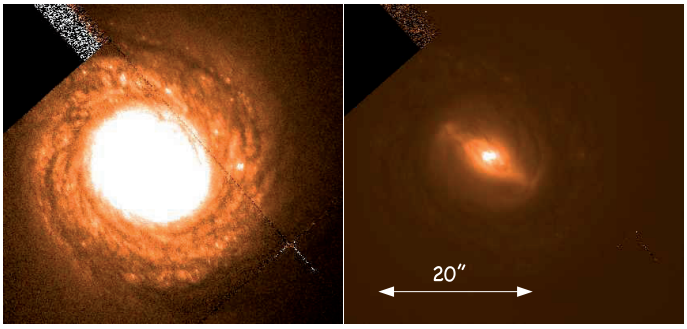

Fig. A.5. HST/WPC2 image of NGC 1317, F606W. Program: 5446, PI: Illingworth. The *left panel* shows how the star-forming "ring" is resolved in many tightly wrapped up spiral arms. The *right panel* shows the visible inner bar. North is up, east to the left.

Fig. A.4, the upper panel is a C-image, showing the dust structures more clearly, while the lower panel is a $C-R$ colour image (compare the colour image of NGC 1316 in Paper I). It is striking that the ellipticity of these two images is so different. We attribute this to the outer secondary bar (Laurikainen et al. 2006), which produces the ellipticity, even though it is not distinct in colour from the overall population.

At higher HST/WPC2 resolution, the ring is resolved into a spiral structure with many tightly wound arms, a point already noted by e.g. Piner et al. (1995) and Lin et al. (2008) for their simulations of star-forming rings in galaxies. The inner radius is about 7″, the outer about 16″, corresponding to 604 pc and 1380 pc, respectively, if we adopt for NGC 1317 the distance of NGC 1316. This is also the region of H_α-emission (Marcum et al. 2001) and it appears black ($C - R \approx 1.2$) on our colour image. Outside this radius one cannot find coherent regions of star formation, but sequences of blueish blobs/spots in the north-eastern and south-western sectors. Because they trace the overall curvature, they very probably represent smaller scale HII-regions, indicating star formation on a lower level than in the inner region. However, they are outside the H_α-map of Marcum et al. (2001). Interestingly, these two sectors build part of a ring. Brighter colours in Fig. A.4 denote dust patterns. It is intriguing that the dust, in the form of filaments, fills an area with a radius of about 5 kpc, but apparently without much star formation, if any. In the very outer parts, NGC 1317 has the appearance of a grand design spiral with two spiral arms dominating. These spiral arms, however, have colours comparable to the bulge colour of NGC 1316, corresponding to populations with ages of about 2 Gyr. NGC 1317 might thus be a case for the longevity of spiral structures. Struck et al. (2011) showed how fast fly-by encounters can produce long-living density waves. Their simulations resemble very closely the appearance of the outer structure of NGC 1317. Moreover, we point out the similarity with the multiple-ring galaxy NGC 6782, which also presents dust lanes resembling spiral arms. The dust is found between two rings of star formation. In the model of Lin et al. (2008) for NGC 6782, the outer ring appears between the corotation radius and the outer Lindblad resonance. In the case of NGC 1317, star formation in the outer ring might have died out and the remaining HII-regions are only the debris of a previous prominent ring. Horellou et al. (2001) note the unusually small HI-disk and mention the possibility that it has been affected by ram pressure, when transversing through the intergalactic hot medium. This then would have happened when the present intermediate-age population was young. Finally, we remark that if N1317 was at exactly the same distance as N1316, one would expect strong tidal forces which would not leave the disk intact and the dust and probably molecular gas quiet with regard to star formation.

Appendix B: Tables

Table B.1 lists all GCs that were selected as point sources in the photometry and thus have an entry in the photometric list of Paper I (Richtler et al. 2012a). The columns are the catalogue number, the coordinates (J2000), the R-magnitude, the colour $C-R$, the heliocentric radial velocity, and its uncertainty. Table B.2 continues the GC list with those objects that are not in the point-source list of Paper I. Their catalogue number derives from the internal catalogue in use and the photometric values of these objects appear only here. The coordinates serve for identification purposes only. Unknown magnitudes and/or colours appear as 99.99. The six double measurements (see Sect. 2.5) are included in Table B.1.

Table B.1. Identification and radial velocities of globular clusters appearing in the catalogue of Paper I.

Id	RA(J2000)	Dec(J2000)	R	$C-R$	Rad. vel.	Error
n1316_gc00250	3:22:13.73	−37:11:56	23.30	1.20	2020	61
n1316_gc00280	3:22:23.21	−37:08:26	22.05	99.99	1656	42
n1316_gc00285	3:22:25.89	−37:12:02	23.50	1.32	1869	56
n1316_gc00286	3:22:26.02	−37:05:17	23.30	1.33	1427	49
n1316_gc00293	3:22:27.50	−37:17:54	23.34	1.44	1800	61
n1316_gc00315	3:22:33.72	−37:18:07	22.87	1.63	1596	51
n1316_gc00319	3:22:35.58	−37:18:09	21.89	1.61	1740	26
n1316_gc00328	3:22:39.10	−37:19:55	22.99	1.25	2122	71
n1316_gc00341	3:22:42.73	−37:21:33	22.41	1.41	1507	170
n1316_gc00383	3:22:52.85	−37:10:26	22.68	1.12	1763	81
n1316_gc00384	3:22:53.00	−37:12:48	22.94	1.31	1960	48
n1316_gc00410	3:22:58.85	−37:08:49	22.86	1.61	1795	63
n1316_gc00420	3:23:01.40	−37:08:34	22.74	1.00	1692	46
n1316_gc00461	3:23:12.47	−37:19:04	22.85	1.26	1782	66
n1316_gc00478	3:23:16.69	−37:20:23	22.57	1.46	1666	42
n1316_gc00485	3:23:18.96	−37:15:04	23.03	1.39	1852	95
n1316_gc00500	3:23:22.69	−37:14:57	22.54	1.83	1814	32
n1316_gc01061	3:22:01.53	−37:15:12	22.59	0.97	2482	79
n1316_gc01075	3:22:02.63	−37:13:20	23.22	1.31	1669	41
n1316_gc01108	3:22:06.91	−37:12:34	21.89	0.96	1944	32
n1316_gc01117	3:22:07.70	−37:15:50	22.30	1.37	1647	55
n1316_gc01177	3:22:15.44	−37:06:07	21.68	1.16	1756	32
n1316_gc01178	3:22:15.87	−37:02:18	21.83	0.37	1831	65
n1316_gc01193	3:22:17.90	−37:16:12	22.96	1.82	1513	53
n1316_gc01214	3:22:20.35	−37:06:22	22.17	1.85	1569	25
n1316_gc01214	3:22:20.35	−37:06:22	22.17	1.85	1641	43
n1316_gc01230	3:22:22.00	−37:09:49	22.78	1.32	1557	43
n1316_gc01273	3:22:26.89	−37:11:59	22.76	1.57	1494	46
n1316_gc01278	3:22:27.23	−37:18:00	23.25	1.47	1829	180
n1316_gc01282	3:22:27.52	−37:12:23	22.35	1.29	1673	73
n1316_gc01304	3:22:29.58	−37:13:26	21.49	1.56	1592	26
n1316_gc01315	3:22:30.70	−37:17:22	23.32	1.18	1446	54
n1316_gc01324	3:22:31.54	−37:15:26	21.25	1.46	1610	21
n1316_gc01350	3:22:34.75	−37:17:41	22.94	1.09	1456	59
n1316_gc01389	3:22:39.07	−37:20:15	22.59	1.56	1802	38
n1316_gc01462	3:22:46.10	−37:09:44	21.67	1.45	1799	38
n1316_gc01524	3:22:50.48	−37:13:02	22.70	1.49	1500	58
n1316_gc01530	3:22:51.15	−37:08:43	23.03	1.45	1722	48
n1316_gc01540	3:22:52.36	−37:09:13	22.91	1.68	1548	103
n1316_gc01586	3:22:56.56	−37:13:54	22.52	1.16	2111	59
n1316_gc01623	3:22:59.72	−37:11:26	20.91	1.18	1874	31
n1316_gc01652	3:23:03.59	−37:11:53	23.21	1.10	2097	81
n1316_gc01695	3:23:09.21	−37:15:32	23.20	1.47	1755	59
n1316_gc01748	3:23:16.64	−37:21:29	22.61	1.58	1828	39
n1316_gc02665	3:22:01.23	−37:16:01	23.16	1.14	1505	44
n1316_gc02736	3:22:06.74	−37:10:58	23.63	0.94	2151	65
n1316_gc02755	3:22:08.05	−37:11:37	22.02	1.69	1751	62
n1316_gc02786	3:22:11.12	−37:09:05	22.31	1.03	1450	88
n1316_gc02802	3:22:12.58	−37:13:27	22.51	1.19	1702	63
n1316_gc02807	3:22:13.23	−37:04:47	23.13	1.17	1544	45
n1316_gc02812	3:22:13.46	−37:12:12	22.88	1.09	1436	64
n1316_gc02834	3:22:15.18	−37:03:10	23.07	1.04	1560	37
n1316_gc02840	3:22:15.51	−37:13:09	21.81	1.56	1552	56
n1316_gc02851	3:22:17.01	−37:15:37	22.32	1.36	1811	31
n1316_gc02855	3:22:17.27	−37:14:59	22.43	1.61	1371	61
n1316_gc02874	3:22:19.18	−37:14:18	21.77	1.05	1640	59
n1316_gc02877	3:22:19.49	−37:02:37	21.52	1.22	1585	39
n1316_gc02888	3:22:20.31	−37:17:04	22.59	1.28	1611	47
n1316_gc02890	3:22:20.41	−37:10:29	22.55	1.26	1656	39
n1316_gc02891	3:22:20.46	−37:05:37	22.17	1.23	2252	70
n1316_gc02891	3:22:20.46	−37:05:37	22.17	1.23	2279	34
n1316_gc02910	3:22:21.77	−37:11:43	21.66	1.44	1626	51

Table B.1. continued.

Id	RA(J2000)	Dec(J2000)	R	$C-R$	Rad. vel.	Error
n1316_gc02950	3:22:25.55	−37:14:37	22.70	1.65	1307	37
n1316_gc02952	3:22:25.77	−37:21:07	22.46	1.31	1542	63
n1316_gc02954	3:22:25.95	−37:19:48	23.56	1.30	1698	42
n1316_gc02958	3:22:26.22	−37:16:16	23.12	1.86	1644	57
n1316_gc02962	3:22:26.53	−37:14:04	22.38	1.06	1557	61
n1316_gc02963	3:22:26.67	−37:10:21	22.26	1.09	1883	61
n1316_gc02969	3:22:27.07	−37:19:27	21.89	1.02	1553	59
n1316_gc02977	3:22:28.21	−37:17:14	22.22	1.44	1626	43
n1316_gc02977	3:22:28.21	−37:17:14	22.22	1.44	1683	41
n1316_gc02991	3:22:29.21	−37:08:30	22.74	1.45	1778	39
n1316_gc02997	3:22:29.42	−37:13:22	21.14	1.45	1976	33
n1316_gc03002	3:22:29.84	−37:11:51	22.93	1.29	1570	56
n1316_gc03004	3:22:29.87	−37:13:53	21.58	1.53	1644	29
n1316_gc03019	3:22:31.10	−37:13:02	20.07	1.49	1830	11
n1316_gc03025	3:22:31.46	−37:18:17	23.58	1.85	1617	165
n1316_gc03027	3:22:31.61	−37:16:07	21.57	1.72	2034	25
n1316_gc03030	3:22:31.70	−37:12:37	20.83	1.55	1623	21
n1316_gc03033	3:22:31.72	−37:13:41	20.83	1.49	1417	15
n1316_gc03041	3:22:32.12	−37:13:10	22.40	1.79	1714	23
n1316_gc03044	3:22:32.39	−37:13:57	21.96	1.26	1777	77
n1316_gc03046	3:22:32.59	−37:12:48	22.14	1.44	1470	37
n1316_gc03055	3:22:32.95	−37:12:15	21.28	1.17	1620	49
n1316_gc03067	3:22:33.69	−37:15:35	23.20	1.53	1792	41
n1316_gc03090	3:22:35.24	−37:16:02	22.12	1.63	1561	32
n1316_gc03096	3:22:35.35	−37:17:58	22.50	1.19	1643	73
n1316_gc03103	3:22:35.83	−37:20:08	22.49	1.42	1731	46
n1316_gc03122	3:22:37.32	−37:16:05	21.88	1.40	1830	41
n1316_gc03132	3:22:38.12	−37:15:36	22.19	1.11	1430	54
n1316_gc03133	3:22:38.13	−37:19:31	22.68	1.40	1443	31
n1316_gc03147	3:22:38.87	−37:19:43	22.37	1.10	1632	74
n1316_gc03151	3:22:39.06	−37:15:13	21.00	1.37	1879	28
n1316_gc03151	3:22:39.06	−37:15:13	21.00	1.37	1939	17
n1316_gc03161	3:22:39.60	−37:15:57	21.42	1.53	1676	20
n1316_gc03192	3:22:41.20	−37:20:51	21.41	1.32	1574	35
n1316_gc03199	3:22:41.51	−37:18:53	23.15	1.10	1788	41
n1316_gc03269	3:22:46.84	−37:14:11	21.70	1.47	1433	66
n1316_gc03280	3:22:47.53	−37:14:25	21.35	1.14	1613	40
n1316_gc03314	3:22:49.15	−37:11:57	21.48	1.09	1831	43
n1316_gc03318	3:22:49.42	−37:11:38	20.33	1.44	1855	25
n1316_gc03327	3:22:49.79	−37:09:06	22.53	1.57	1880	77
n1316_gc03332	3:22:50.14	−37:13:15	22.39	1.20	2048	105
n1316_gc03336	3:22:50.85	−37:12:25	20.95	1.27	1618	27
n1316_gc03338	3:22:51.08	−37:12:31	22.24	1.03	1778	54
n1316_gc03351	3:22:51.79	−37:11:05	21.31	1.14	1685	38
n1316_gc03374	3:22:53.24	−37:10:32	21.29	1.06	1635	41
n1316_gc03381	3:22:53.75	−37:11:14	21.76	1.13	1714	33
n1316_gc03394	3:22:54.37	−37:13:40	23.28	1.21	2089	59
n1316_gc03397	3:22:54.58	−37:11:20	21.86	1.65	1813	34
n1316_gc03411	3:22:55.47	−37:09:48	22.30	1.07	1966	61
n1316_gc03417	3:22:56.15	−37:11:23	21.36	1.37	1896	36
n1316_gc03422	3:22:56.36	−37:09:22	21.48	1.04	1948	87
n1316_gc03451	3:22:58.69	−37:14:19	21.98	1.10	1872	78
n1316_gc03541	3:23:06.46	−37:14:44	22.88	1.04	1525	48
n1316_gc03580	3:23:08.68	−37:06:43	23.20	0.95	1138	66
n1316_gc03632	3:23:12.97	−37:09:17	21.88	1.41	1911	42
n1316_gc03667	3:23:16.59	−37:15:21	21.74	1.03	1606	50
n1316_gc03723	3:23:21.07	−37:10:07	22.46	0.93	1872	40
n1316_gc04101	3:22:09.78	−37:15:17	22.52	1.40	1353	64
n1316_gc04128	3:22:24.66	−37:15:41	22.45	1.57	1839	47
n1316_gc04128	3:22:24.66	−37:15:41	22.45	1.57	1937	30
n1316_gc04132	3:22:25.60	−37:10:42	22.23	1.34	1744	42
n1316_gc04138	3:22:26.15	−37:17:28	22.01	1.17	1621	34
n1316_gc04138	3:22:26.15	−37:17:28	22.01	1.17	1635	46
n1316_gc04146	3:22:28.32	−37:15:25	23.19	1.38	1466	57

Table B.1. continued.

Id	RA(J2000)	Dec(J2000)	R	$C-R$	Rad. vel.	Error
n1316_gc04149	3:22:29.08	−37:14:12	21.54	1.55	1629	32
n1316_gc04150	3:22:30.67	−37:14:17	20.58	1.38	1389	32
n1316_gc04155	3:22:32.60	−37:16:02	21.99	1.42	1688	52
n1316_gc04224	3:22:49.14	−37:09:19	22.03	1.66	2059	29
n1316_gc04238	3:22:53.28	−37:10:58	21.92	1.25	2008	49
n1316_gc04518	3:22:37.86	−37:18:03	20.94	1.26	1705	17
n1316_gc03579	3:23:08.63	−37:04:50	21.16	1.65	1980	30
n1316_gc03505	3:23:03.07	−37:08:26	19.74	1.18	1812	18
n1316_gc04308	3:23:23.05	−37:10:27	21.00	1.15	1887	34
n1316_gc01752	3:23:16.64	−37:10:49	20.57	1.12	1771	38
n1316_gc03505	3:23:03.13	−37:08:27	19.74	1.18	1749	15
n1316_gc03384	3:22:53.89	−37:10:14	19.14	1.39	1976	10
n1316_gc01293	3:22:28.88	−37:18:15	20.89	1.75	1825	12
n1316_gc03088	3:22:35.23	−37:19:18	21.16	1.55	1838	13
n1316_gc03047	3:22:32.64	−37:14:56	20.75	1.39	1607	19

Table B.2. Identification and radial velocities of globular clusters without entry in the photometric catalogue in Paper I.

Id	RA(J2000)	Dec(J2000)	R	$C-R$	Rad. vel.	Error
n1316_gc02855	3:21:58.70	−37:12:50	23.40	1.11	1925	61
n1316_gc02965	3:22:03.39	−37:14:34	22.43	1.59	1554	33
n1316_gc03030	3:22:06.46	−37:08:01	22.59	1.64	1662	55
n1316_gc20839	3:22:07.68	−37:05:13	22.52	1.38	821	36
n1316_gc00662	3:22:08.47	−37:13:56	22.50	1.66	1708	96
n1316_gc03281	3:22:17.03	−37:06:04	22.92	1.93	746	50
n1316_gc20852	3:22:19.35	−37:08:53	22.72	-0.03	2139	64
n1316_gc20726	3:22:26.75	−37:08:42	21.96	1.77	2224	64
n1316_gc00834	3:22:27.27	−37:12:54	22.40	1.41	1625	24
n1316_gc00848	3:22:29.06	−37:13:48	22.71	1.42	1583	51
n1316_gc10314	3:22:29.26	−37:16:11	22.95	1.24	1145	55
n1316_gc11298	3:22:34.35	−37:20:29	22.84	1.50	1460	76
n1316_gc20470	3:22:34.62	−37:17:01	22.57	0.90	2140	63
n1316_gc20439	3:22:37.52	−37:18:58	20.83	1.52	1711	20
n1316_gc20440	3:22:38.04	−37:18:46	21.71	0.22	1662	20
n1316_gc20552	3:22:41.54	−37:16:30	21.97	1.27	1715	30
n1316_gc20426	3:22:42.42	−37:16:48	99.99	99.99	1484	26
n1316_gc04094	3:22:46.04	−37:10:28	22.55	1.73	737	53
n1316_gc04140	3:22:47.56	−37:10:39	22.28	1.50	1820	53
n1316_gc20237	3:22:48.76	−37:10:53	22.06	1.09	1983	72
n1316_gc20282	3:22:48.94	−37:14:49	21.84	1.74	1497	78
n1316_gc08412	3:22:50.85	−37:12:25	20.95	1.28	1619	27
n1316_gc08569	3:22:55.53	−37:12:17	23.30	1.16	1510	60
n1316_gc04534	3:23:00.26	−37:08:58	23.04	1.36	2023	50
n1316_gc08693	3:23:00.35	−37:06:11	23.31	1.48	1821	53
n1316_gc20118	3:23:03.76	−37:04:29	21.45	1.30	1976	45
n1316_gc04633	3:23:04.61	−37:04:55	22.99	1.08	1318	66
n1316_gc08822	3:23:04.84	−37:03:49	22.28	1.08	2917	47
n1316_gc20231	3:23:06.55	−37:10:43	19.57	1.48	1596	9
n1316_gc08860	3:23:06.70	−37:14:34	23.23	1.62	1212	61
n1316_gc08863	3:23:06.75	−37:10:02	22.52	1.40	1661	63
n1316_gc20330	3:23:07.69	−37:16:53	99.99	99.99	1798	86
n1316_gc08918	3:23:08.98	−37:18:50	22.35	1.14	1774	59
n1316_gc01232	3:23:09.96	−37:18:27	22.65	1.45	1255	65
n1316_gc20313	3:23:11.47	−37:14:50	22.21	1.75	1773	56
n1316_gc08973	3:23:11.72	−37:17:30	23.07	1.48	1563	58
n1316_gc04772	3:23:12.22	−37:05:04	23.42	1.64	2322	78
n1316_gc20340	3:23:15.02	−37:17:17	22.42	1.33	1950	66
n1316_gc20343	3:23:17.95	−37:17:48	22.16	1.28	2473	63
n1316_gc20151	3:23:18.46	−37:07:17	99.99	99.99	1078	49
n1316_gc20161	3:23:20.33	−37:08:31	20.09	1.04	1888	36
n1316_gc01347	3:23:21.56	−37:06:38	24.02	0.93	1564	82